

A self-consistent explanation of the MeV line in GRB 221009A unveils a dense circum-stellar medium

Om Sharan Salafia^{1,2}, Annalisa Celotti^{3,1,4,5}, Emanuele Sobacchi^{6,7}, Lara Nava¹, Gor Oganesyan^{6,7}, Giancarlo Ghirlanda¹, Stella Boula¹, Maria Edvige Ravasio^{8,9,1}, Gabriele Ghisellini¹

¹ INAF – Osservatorio Astronomico di Brera, via Emilio Bianchi 46, I-23807 Merate (LC), Italy

² INFN – sezione di Milano-Bicocca, Piazza della Scienza 3, I-20126 Milano (MI), Italy

³ SISSA, via Bonomea 265, I-34136 Trieste, Italy

⁴ INFN – sezione di Trieste, via Valerio 2, I-34127, Trieste, Italy

⁵ IFPU – Institute for Fundamental Physics of the Universe, via Beirut 2, I-34151 Trieste, Italy

⁶ Gran Sasso Science Institute, viale F. Crispi 7, L’Aquila, I-67100, Italy

⁷ INFN – Laboratori Nazionali del Gran Sasso, L’Aquila, I-67100, Italy

⁸ Institute of Space Sciences (ICE, CSIC), Campus UAB, Carrer de Can Magrans s/n, E-08193, Barcelona, Spain

⁹ Department of Astrophysics/IMAPP, Radboud University, PO Box 9010, 6500 GL Nijmegen, The Netherlands

Received xxx; accepted xxx

ABSTRACT

GRB 221009A has been the brightest gamma-ray burst (GRB) observed to date, and its afterglow has been characterised with unprecedented detail at TeV energies by LHAASO. Quite puzzlingly, it is also the most energetic GRB known. Among the riddles posed by this mysterious source, however, the sheer energetics are hardly the most intriguing: an unprecedented, narrow, luminous emission line at around 10 MeV has been uncovered by a detailed spectral analysis of *Fermi*/GBM data immediately following the brightest peak in the GRB prompt emission and the peak of the TeV afterglow. As noted in the discovery article, the temporal evolution of the line properties can be explained as being due to high-latitude emission from a geometrically thin, relativistically expanding shell where annihilation of a large number of electron-positron pairs took place. We show that this interpretation yields stringent constraints on the properties of such shell, that point to a process that happens at radii typical of external shocks. We then demonstrate that the shell could have been the blastwave associated with the GRB precursor, with the line arising after pair loading of such blastwave as it was illuminated by the bright and hard radiation of the GRB main event. The scenario, which also explains the abrupt initial rise of the LHAASO afterglow, requires the progenitor of the GRB to have been surrounded by a circum-stellar medium (CSM) extending out to a few 10^{15} cm, with a density $n_{\text{ext}} \sim 10^8 - 10^9 \text{ cm}^{-3}$ reminiscent of those found from studies of Type IIn supernovae. This provides a precious clue to the nature of the progenitor of this peculiar GRB, which could also be present in other bursts that feature a long quiescence followed by a bright emission episode with a hard spectrum.

Key words. relativistic astrophysics – gamma-ray bursts: general – gamma-ray burst: individual: GRB 221009A – stars: circumstellar matter

1. Introduction

Despite decades of research and a growing sample of well-characterised examples, gamma-ray bursts (GRBs, [Kumar & Zhang 2015](#)) remain among the most elusive astronomical sources. The association of some members of this class with core-collapse supernovae ([Galama et al. 1998](#)) and studies of their host galaxies ([Vergani et al. 2015](#)) clearly point to massive star progenitors, but the actual properties of the progenitor stars, and how these are linked to the observed GRB properties (such as energetics, duration, spectral features) remain poorly understood. In part, this is a consequence of the fact that the mechanism behind GRB ‘prompt’ emission (i.e. the initial, highly variable emission that is detected through space-based hard-X-ray and soft gamma-ray observatories) is still not well constrained. Even the longer-lasting ‘afterglow’, whose evolution is less erratic, and whose underlying mechanisms are better understood ([Panaitescu & Kumar 2000](#)), often presents features that are not easily interpreted within the standard picture.

A particularly puzzling example is the extremely bright GRB 221009A (the brightest ever recorded to date – [Malesani](#)

[et al. 2025](#)), which was detected on October 9, 2022 by virtually all X-ray and gamma-ray detectors on spacecraft, including the Gamma-ray Burst Monitor (GBM) and the Large Area Telescope (LAT) onboard *Fermi* ([Lesage et al. 2023; Axelsson et al. 2025](#)), the Konus detector onboard *WIND* ([Frederiks et al. 2023](#)) and the GECAM-C cubesat ([Zhang et al. 2024a](#)). Throughout this article, we take the *Fermi*/GBM trigger time, 13:16:59.9 universal time (UT), as our observer-frame reference time. The gamma-ray light curve featured an initial pulse of about 10 s, followed by a long apparent quiescence of about 180 s, after which a highly variable and bright emission event (showing multiple peaks, some of which saturated the GBM detectors) took place, lasting hundreds of seconds.

At a UT time corresponding to 230 seconds after the *Fermi*/GBM trigger, the Water Cherenkov Detector Array (WCDA) of the Large High Altitude Air Shower Observatory (LHAASO, [LHAASO Collaboration et al. 2023](#)) detected a very high-significance, transient emission at TeV photon energies, coming from a direction consistent with the location of the GRB. The TeV light curve, characterised with unprecedented detail,

showed a very sharp rise of a few seconds, followed by a slightly gentler rise of about 10 seconds, and then a smooth decay (see bottom panel of Fig. 1).

At around 280 s, shortly after the brightest peak of the prompt emission and the onset of the TeV afterglow, Rava-sio et al. (2024) (hereafter R24) discovered an unprecedented, highly significant, narrow emission feature with a luminosity of about 10^{30} erg s $^{-1}$ and a central photon energy slightly in excess of 10 MeV. A detailed spectral analysis showed an evolution of the line properties towards lower luminosity and photon energy during the subsequent minute, after which the feature could not be detected anymore. A statement by the *Fermi*/GBM team (Burns et al. 2024) confirmed the presence of the feature in the data and excluded an instrumental artifact. The feature was further analysed and characterised in subsequent works (Axelsson et al. 2025; Zhang et al. 2024a), and a hint of a related feature was reported in Konus-WIND data (Frederiks et al. 2023).

In this paper, we propose a scenario to explain the emergence of the line, its timing, its properties and their evolution. As we will demonstrate, the scenario provides a self-consistent explanation of various features of the prompt emission and afterglow of this GRB, and yields a clue about the nature of its progenitor. In Section 2 we show that the evolution of the line properties can be interpreted as high-latitude emission (HLE) from a shell in relativistic expansion within which mass-annihilation of a large number of electron-positron (e^-e^+) pairs took place, as already proposed by R24, Zhang et al. (2024a,b), and Pe'er & Zhang (2024) (see Liu et al. 2025 for an alternative scenario). We show that this interpretation poses quite stringent constraints on the number of annihilating pairs and on the bulk Lorentz factor of the shell, and also on the observer-frame time at which the annihilation started. In Section 3 we describe our proposed scenario for the production of the required number of pairs and their mass-annihilation and demonstrate its general feasibility. In Section 4 we describe our detailed model of the process that leads to the pair enrichment and acceleration of the pair-loaded shell, and derive the constraints on the model parameter space imposed by the HLE interpretation. Finally, in Section 5 we discuss our results and their consequences on the properties of the progenitor. We provide a compact summary and our conclusions in Section 6.

Throughout this article, we employ the usual notation $Q_x = Q_{\text{cgs}}/10^x$, where Q is any quantity and Q_{cgs} is its value in cgs units. Primed quantities are measured in the fluid frame. When a cosmology is needed, we adopt a flat Λ CDM model with Planck Collaboration et al. (2020) parameters. The redshift of GRB 221009A, determined spectroscopically, is $z = 0.151$ (Malesani et al. 2025).

2. Interpreting the line evolution as due to high latitude emission

Observationally, as shown¹ in the two middle panels of Figure 1, the temporal evolution of the line properties is consistent with $L_{\text{line}} \propto (t - t_0)^{-3}$ and $h\nu_{\text{line}} \propto (t - t_0)^{-1}$ if the reference time t_0 is taken close to the peak of the GRB 221009A prompt emission, $220 \lesssim t_0/\text{s} \lesssim 240$ (R24). This is confirmed also by the independent analysis of Zhang et al. (2024a). While the latter analysis raises reasonable concerns because it makes use of formally

saturated *Fermi*/GBM data (Lesage et al. 2023), the *Fermi*/GBM Collaboration considers it acceptable, at least in part (Burns et al. 2024). In addition, Frederiks et al. (2023) reported about a possible hint at the presence of the line in Konus-WIND spectra covering the interval from 225 to 233 s. Differently from their assessment, we find that the photon energy and luminosity of such tentative line are not consistent with the extrapolation of the aforementioned power laws (Fig. 1, panels b and c).

This temporal evolution can be interpreted (R24) as being due to the HLE effect that arises when a spherical source produces a brief flash of radiation while expanding at relativistic speed. If the emission duration of the flash satisfies $\Delta t_{\text{em}} \ll r/c$, where r is the emission radius, then the temporal evolution of the observed radiation is set by the delayed arrival of photons emitted at increasing latitudes (and with decreasing Doppler factors) with respect to the source axis parallel to the line of sight (Kumar & Panaiteescu 2000). In Appendix A we give a derivation that clarifies some aspects of this effect with respect to that in the original paper.

2.1. Requirements set by HLE in the e^+e^- pair annihilation scenario

If a narrow emission line with a central photon energy $h\nu'_{\text{line}}$ (as measured in the rest frame of the emitting material) is produced within a geometrically thin spherical shell of radius r over a time shorter than r/c (c being the speed of light), while the spherical shell is expanding with a bulk Lorentz factor $\Gamma \gg 1$, then the evolution of the line luminosity and photon energy with the observer-frame time t_{obs} is set by the HLE effect, and is given by (see Appendix A)

$$L_{\text{line}}(t_{\text{obs}}) \sim \frac{2E_{\text{rad}}/t_{\text{ang}}}{[1 + (t_{\text{obs}} - t_0)/(1 + z)t_{\text{ang}}]^3}, \quad (1)$$

$$h\nu_{\text{line}}(t_{\text{obs}}) \sim \frac{2\Gamma h\nu'_{\text{line}}/(1 + z)}{1 + (t_{\text{obs}} - t_0)/(1 + z)t_{\text{ang}}}, \quad (2)$$

where E_{rad} is the total radiated energy, t_0 is the arrival time of the first photon and $t_{\text{ang}} = r/2\Gamma^2 c$ is the ‘angular’ time scale. In words, the HLE effect produces a nearly constant luminosity $L_{\text{line}} \sim E_{\text{rad}}/t_{\text{ang}}$ and line photon energy $h\nu_{\text{line}} \sim \Gamma h\nu'_{\text{line}}/(1 + z)$ as long as $t_{\text{obs}} - t_0 < (1 + z)t_{\text{ang}}$, followed by a power law decline $L_{\text{line}} \propto (t_{\text{obs}} - t_0)^{-3}$ and $h\nu_{\text{line}} \propto (t_{\text{obs}} - t_0)^{-1}$.

2.1.1. Constraints on radius and bulk Lorentz factor

If the line is attributed to electron-positron pair annihilation, and its evolution is due to the HLE effect, then some stringent constraints on the properties of the thin shell can be deduced as follows. At $t_{\text{obs}} - t_0 \gg (1 + z)t_{\text{ang}}$ we have, from Eq. 2,

$$\frac{t_{\text{obs}} - t_0}{(1 + z)t_{\text{ang}}} \sim \frac{2\Gamma h\nu'_{\text{line}}}{(1 + z)h\nu_{\text{line}}} = \frac{2\Gamma m_e c^2}{(1 + z)h\nu_{\text{line}}}, \quad (3)$$

where we assumed $h\nu'_{\text{line}} = m_e c^2$. Using the luminosity evolution, Eq. 1, we then have

$$L_{\text{line}} \sim \frac{8N_{\pm}\Gamma^3 m_e c^3}{r} \left[\frac{2\Gamma m_e c^2}{(1 + z)h\nu_{\text{line}}} \right]^{-3} = \frac{N_{\pm} m_e c^3}{r} \left[\frac{m_e c^2}{(1 + z)h\nu_{\text{line}}} \right]^{-3}, \quad (4)$$

¹ The orange error bars in Fig. 1 reflect the results reported in table 9 of Axelsson et al. (2025), but we note that these seem to conflict with the visualization in their figure 8, where the line evolution seems rather smooth and monotonic.

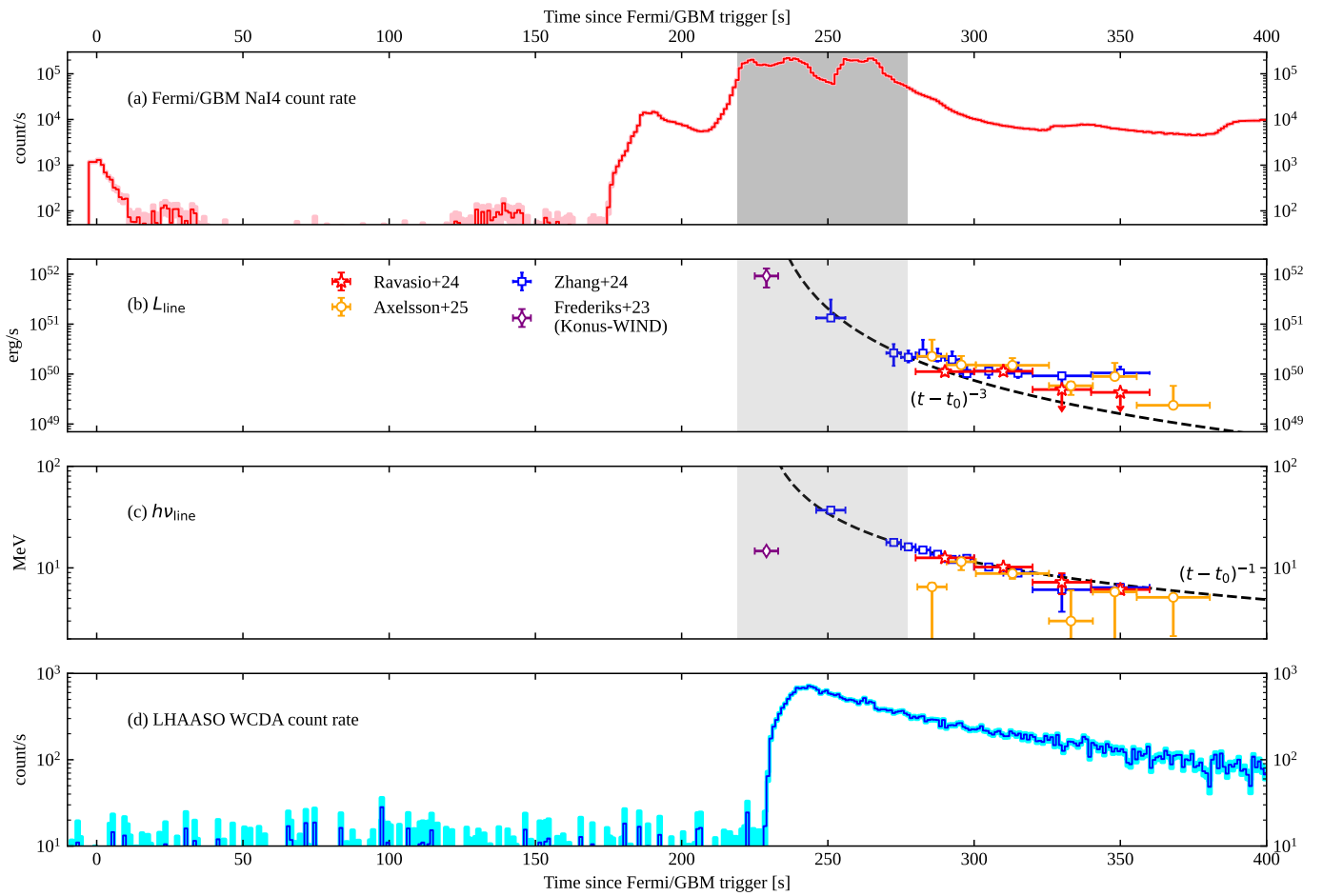


Fig. 1. GRB 221009A light curves and narrow line properties. **Panel (a):** background-subtracted count rate light curve of the fourth sodium-iodide (NaI) detector of *Fermi*/GBM (red histogram, sensitive to emission in the 8 keV – 1 MeV band). The pink shading shows the one-sigma-equivalent uncertainty, assuming Poisson-distributed background counts. The gray-shaded area shows the ‘Bad Time Interval’ (BTI) during which the GBM detectors were affected by saturation. **Panel (b):** Gaussian line luminosity evolution. Error bars show the estimated Gaussian line luminosity according to the analysis of GBM data reported in R24 (red stars), Axelsson et al. (2025, orange circles), Zhang et al. (2024a, blue squares), and that of the tentatively detected line in Konus-WIND data (Frederiks et al. 2023, purple diamond). The BTI time range (only relevant to GBM) is reported with a lighter gray shading. **Panel (c):** same as panel (b), but for the line central photon energy. **Panel (d):** LHAASO WCDA count rate light curve (LHAASO Collaboration et al. 2023). The cyan shading shows the one-sigma-equivalent uncertainty, assuming Poisson-distributed background counts.

where we assumed $E_{\text{rad}} = 2\Gamma m_e c^2 N_{\pm}$, that is, an energy $2\Gamma m_e c^2$ contributed by each of the N_{\pm} annihilating pairs². This allows us to express the total number of annihilating pairs as a function of measured observables, plus the radius r as the only free parameter,

$$N_{\pm} \approx 1.8 \times 10^{57} r_{16} L_{\text{line},50} \left(\frac{h\nu_{\text{line}}}{12.6 \text{ MeV}} \right)^{-3} \left(\frac{1+z}{1.15} \right)^{-3}, \quad (5)$$

where the reference values for L_{line} and $h\nu_{\text{line}}$ are based on the analysis of the first significant time bin of R24.

From Eq. 3 and the definition of t_{ang} , we could also derive a constraint on the bulk Lorentz factor,

$$\Gamma_{\text{HLE}} \sim \frac{r}{c(t_{\text{obs}} - t_0)} \frac{m_e c^2}{h\nu_{\text{line}}} \approx 225 r_{16} \left(\frac{t_{\text{line}} - t_0}{60 \text{ s}} \right)^{-1} \left(\frac{h\nu_{\text{line}}}{12.6 \text{ MeV}} \right)^{-1}, \quad (6)$$

² This implies cold pairs and neglects three-photon annihilation, which concerns only a small fraction of the pairs – e.g. Svensson 1987.

where t_{line} here refers to the time at which $h\nu_{\text{line}}$ is measured (the central time of the first significant bin analysed in R24 is $t_{\text{line}} = 290$ s) and we took $t_0 = 230$ s as reference.

As stated above, the HLE interpretation requires the emission time to be shorter than r/c . In the pair annihilation scenario, this in turn requires the comoving annihilation time $t'_{\text{ann}} \sim 8n'_{\pm}/3\sigma_{\text{T}} c n'_{\pm}^{-2}$ (where n'_{\pm} is the comoving pair number density, and we assume cold pairs) to be shorter than $r/\Gamma c$. We can get some insight from this requirement if we express the shell comoving thickness as $\Delta r' = \xi r/\Gamma$, so that the comoving volume is $V' = \xi 4\pi r^3/\Gamma$. Here ξ is a dimensionless constant, with typical values $\xi \sim 0.1 - 0.3$ for the downstream of an external shock (Blandford & McKee 1976, hereafter BM76). Then $n'_{\pm} = N_{\pm}/V'$ and the $t'_{\text{ann}} < r/\Gamma c$ inequality becomes, using Eq. 5,

$$\xi < \frac{3\sigma_{\text{T}} L_{\text{line}}}{32\pi m_e c^3 r} \left[\frac{m_e c^2}{(1+z)h\nu_{\text{line}}} \right]^3 \approx 0.4 r_{16}^{-1} L_{\text{line},50} \left(\frac{h\nu_{\text{line}}}{12.6 \text{ MeV}} \right)^{-3} \left(\frac{1+z}{1.15} \right)^{-3}. \quad (7)$$

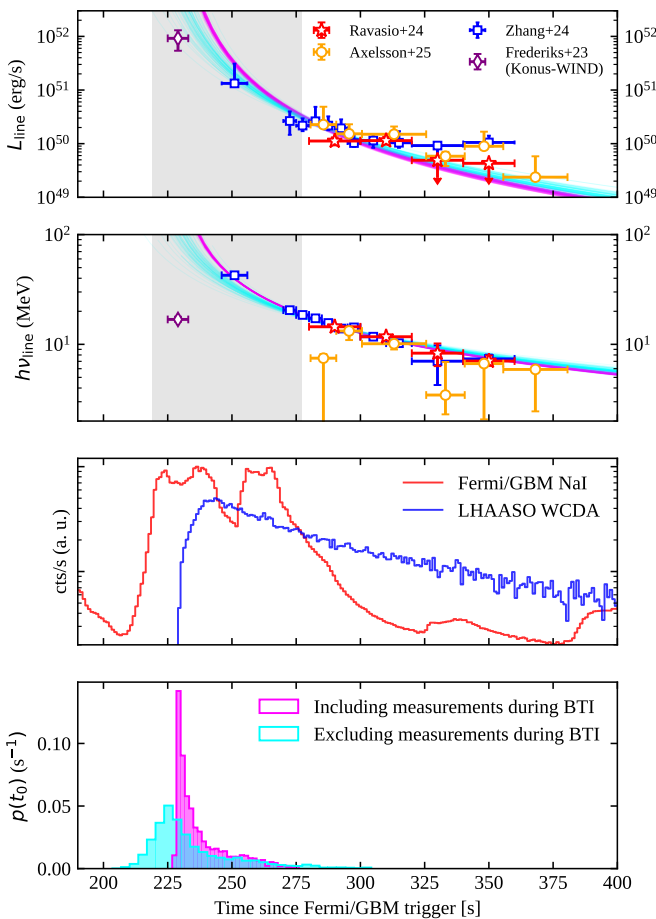


Fig. 2. HLE model fit results. From top to bottom: in the first (second) panel, purple lines show the evolution of L_{line} ($h\nu_{\text{line}}$) from one hundred posterior samples of the HLE model fitted to the evolution inferred from the observations (shown by the error bars – see text), including data in the BTI (grey shaded area). Cyan lines show the corresponding result when such data is excluded. The third panel shows the *Fermi*/GBM and LHAASO WCDA light curves as temporal references. In the last panel, the purple and cyan histograms show the posterior probability of the HLE start time t_0 inferred from the same two model fitting procedures.

This result shows that, were our pairs confined within the typical volume of an external shock downstream at $r \lesssim \text{few} \times 10^{16} \text{ cm}$, they would annihilate fast enough for the annihilation line emission to be in the HLE regime.

2.1.2. Constraint on the annihilation start time t_0

The interpretation of the line as HLE of e^+e^- pair annihilation implies some additional constraints on t_0 , r and Γ , which follow from two requirements: (i) the start time t_0 must be earlier than the first observation of the line, and (ii) the HLE-predicted evolution must reproduce that inferred from the observations. These conditions are somewhat delicate, because of saturation of the GBM detectors during the ‘Bad Time Interval’ (BTI, from 219 to 277 s, as given in [Lesage et al. 2023](#), and shown here with gray shading in Fig. 1) and because different analyses do not fully agree on the inferred properties of the line, as shown by the presence of incompatible error bars in Fig. 1. A possible reason for the discrepant results at times $t \gtrsim 320$ s could reside in the difficulty in modelling the continuum: as shown by the analysis reported by [R24](#), also confirmed by [Zhang et al. \(2024a\)](#) and [Axelsson et al. \(2025\)](#), at these times an additional emission component is present, on top of the usual prompt emission continuum, which is probably related to the emergence of the afterglow. Different choices in the parametrisation of the emission components and other technical details could have led to inconsistent results.

With these caveats in mind, we fitted the simple HLE physical model (Eqs. 1 and 2) to two sub-samples of the data points shown in Fig. 1, selected as follows. We ignored data beyond $t = 320$ s and we did not take into account the results from [Axelsson et al. \(2025\)](#), because of the discontinuous $h\nu_{\text{line}}$ implied there, which is in contradiction with the assessment from the other analyses) and from [Frederiks et al. \(2023\)](#), because of the low significance). Both sub-samples hence comprise data-points from [R24](#) and [Zhang et al. \(2024a\)](#): in one case, we conservatively excluded the line properties inferred by [Zhang et al. \(2024a\)](#) using data earlier than $t = 275$ s (i.e. BTI data), while in the other case we included all their datapoints. Appendix B provides technical details about the procedure used. The results are summarised in Table 1. In Fig. 2 we also show with cyan (magenta) lines 100 posterior samples of the model line luminosity and photon energy evolution obtained from the fit excluding (including) the data within the BTI. The associated posterior probability density of t_0 is shown with the corresponding color in the bottom panel.

Within the allowed range, as expected based on the analytical reasoning in the previous section, the preferred values of Γ and N_{\pm} are highly correlated with r and can be summarised as $\Gamma = (194 \pm 13)r_{16}$ and $N_{\pm} = (3.0 \pm 0.19) \times 10^{57}r_{16}$ when excluding BTI data, or $\Gamma = (215 \pm 3.4)r_{16}$ and $N_{\pm} = (2.8 \pm 0.17) \times 10^{57}r_{16}$ when including it. These results, while formally in a slight tension, are qualitatively consistent with those obtained in the previous section. The model fitting produces an additional, informative constraint on the arrival time of the first photon, $t_0 = 234 \pm 17$ s if BTI data are excluded, or $t_0 = 238 \pm 10$ s if included. In both cases, this is strikingly close to the initial sharp rise in the LHAASO light curve, as shown in Fig. 2.

These results show that the HLE interpretation of the line evolution, within the e^+e^- pair annihilation scenario, requires the spherical shell where the annihilation took place to be quite rapidly expanding, geometrically as thin as an external shock (or thinner), and to contain a large number of pairs. Its radius must have been somewhere between about 10^{15} cm up to around $4 \times 10^{16} \text{ cm}$, and the arrival time of the first photon must have been within the brightest peak of the prompt emission and close to the sharp rising phase at the beginning of the LHAASO afterglow.

2.2. Pair multiplicity

In the range of radii derived above, the external shock that arises from the interaction of the GRB ejecta with the external medium is expected to become important. Let us assume an external medium whose composition is described by an electron fraction Y_e ($Y_e = 1$ for pure hydrogen, $Y_e \sim 0.5$ for other elements), with a number density profile $n_{\text{ext}}(r) = A_{\star}(r/r_{\star})^{-k}$, where $A_{\star} = 1 A_{\star,0} \text{ cm}^{-3}$ is the number density at a reference radius $r_{\star} \equiv 5.5 \times 10^{17} \text{ cm}$. This definition ensures that our reference density $A_{\star} = 1 \text{ cm}^{-3}$ matches that of a typical interstellar medium (ISM) if $k = 0$, and that of a typical Wolf-Rayet stellar wind ([Chevalier & Li 2000](#)) if $k = 2$. If $k = 0$, then n_{ext} is equal to A_{\star} at all radii, and we will use the former symbol for clarity. If the pairs are created downstream of an external shock, at a radius r this would have swept a number of electrons $N_e = 4\pi Y_e A_{\star} r^{3-k} r_{\star}^k / (3 - k)$. The pair multiplicity, that is, the

Table 1. Summary of HLE parameter constraints from model fitting.

Parameter	Excluding BTI		Including BTI	
	Mean \pm st. dev.	90% C.R.	Mean \pm st. dev.	90% C.R.
$x_0 = r_{16}$	1.2 ± 1.3	[0.10, 4.2]	1.3 ± 1.2	[0.13, 3.9]
$x_1 = \Gamma/r_{16}$	194 ± 13	[173, 214]	215 ± 3.4	[210, 220]
$x_2 = N_{\pm,57}/r_{16}$	3.0 ± 0.19	[2.7, 3.3]	2.8 ± 0.17	[2.5, 3.1]
Γ	240 ± 240	[20, 800]	270 ± 260	[27, 830]
$N_{\pm,57}$	3.7 ± 3.9	[0.30, 12]	3.6 ± 3.4	[0.33, 11]
t_0/s	234 ± 17	[217, 270]	238 ± 10	[229, 260]

Notes. Each line refers to a model parameter (see Appendix B) or a quantity derived from a combination of model parameters, the two cases being separated with a horizontal line. For each line, we report the mean, standard deviation, and symmetric 90% credible range (comprised between the 5th and 95th percentiles) of the posterior samples obtained by fitting the line properties either excluding the data from the BTI or including it.

number of leptons per external electron that need to be produced in the HLE scenario (focussing on the most relevant cases $k = 0$ and $k = 2$) is

$$Z_{\pm, \text{HLE}} = \frac{N_e + 2N_{\pm}}{N_e} \approx 1 + \begin{cases} 8.5 \times 10^6 Y_e^{-1} r_{16}^{-2} n_{\text{ext},2}^{-1} L_{\text{line},50} \left(\frac{h\nu_{\text{line}}}{12.6 \text{ MeV}} \right)^{-3} \left(\frac{1+z}{1.15} \right)^{-3}, & k = 0; \\ 9.4 \times 10^4 Y_e^{-1} A_{\star,0}^{-1} L_{\text{line},50} \left(\frac{h\nu_{\text{line}}}{12.6 \text{ MeV}} \right)^{-3} \left(\frac{1+z}{1.15} \right)^{-3}, & k = 2. \end{cases} \quad (8)$$

This very high multiplicity requires a scenario where an efficient mechanism of pair production can operate at the required radii. In the following, we set out to construct such a scenario.

3. The scenario

A peculiar feature of GRB 221009A is the presence of a ‘precursor’: the emission starts with a short burst lasting a few seconds, with an energy $E_{\gamma, \text{pre}} \sim 10^{51}$ erg radiated in gamma-rays, followed by a quiescent period of rest-frame duration $\Delta t_{\text{pre}} \sim 160 \Delta t_{\text{pre},2.2}$ s, after which the main emission (which delivers a 10⁴-fold larger energy – [Frederiks et al. 2023](#)) starts off (Fig. 1, panel a). The precursor, which constitutes by itself a relatively powerful gamma-ray burst, must be associated with a relativistic outflow. The expansion of the ejecta of such an outflow into the external medium drives a relativistic blastwave ([Blandford & McKee 1976](#), BM76 hereafter). When the main event photons illuminate this blastwave with their extremely large luminosity and hard spectrum, they can modify the composition and dynamics by interacting with leptons in the shocked material. We envisage a scenario where this ‘illumination phase’ leads to copious pair production, through a similar process as that proposed by [Madau & Thompson \(2000\)](#) and [Thompson & Madau \(2000\)](#), but with the precursor blastwave as a target, instead of a cold external medium. In the following we show that, under some conditions, the illumination phase ends with (or is followed by) the ‘pair bubble bursting’, that is, mass-annihilation of the created pairs. This leads to the appearance of the line, which is seen to evolve due to the HLE effect. In this scenario, the alignment of the start time t_0 of the HLE with the onset of the LHAASO afterglow has a natural explanation: before colliding with the precursor blastwave, the main event ejecta expanded in vacuum, hence they did not contribute to the afterglow. With the collision, the energy in the external shock increases by orders of magnitude, causing a sudden, sharp rise in the luminosity. The collision happens right after the illumination phase, therefore it is almost contemporaneous to the pair bubble bursting.

In Fig. 3 we sketch the main phases of the proposed scenario, along with a depiction of the time evolution of the radii of the precursor ejecta and gamma-rays, the precursor blastwave, and of the main event ejecta and gamma-rays. In the following we describe in detail the initial conditions of the illumination phase and the requirements that the scenario imposes on the properties of the external medium and of the precursor ejecta.

3.1. Precursor blastwave radius and Lorentz factor at the start of the illumination phase

Let us indicate with $E_{\text{pre}} = 10^{52} E_{\text{pre},52}$ erg the energy in the precursor ejecta and with $\Gamma_{\text{ej,pre}}$ their bulk Lorentz factor. The associated ‘deceleration’ time (measured in the rest frame of the progenitor) is

$$t_{\text{dec}} \approx \left(\frac{(3-k)E_{\text{pre}}}{4\pi A_{\star} r_{\star}^k m_p c^2 \Gamma_{\text{ej,pre}}^2 c^{3-k}} \right)^{1/(3-k)}, \quad (9)$$

where m_p is the proton rest mass. The deceleration, which corresponds to the time when the most of the ejecta energy is deposited into a relativistic blastwave that expands into the external medium, is seen to happen at a time $t_{\text{dec,obs}} \approx (1+z)t_{\text{dec}}/\Gamma_{\text{ej,pre}}^2$ by a distant observer.

Let us focus on panel (g) of Fig. 3. At $t \ll t_{\text{dec}}$ the precursor ejecta (purple) propagate at constant speed and produce a photon pulse (the precursor emission – yellow). At a time $t > t_{\text{dec}}$, the ejecta deposited all their energy into a blastwave (red) whose leading shock propagates with a Lorentz factor (BM76)

$$\Gamma_s(t) \approx \left[\frac{(17-4k)E_{\text{pre}}}{8\pi A_{\star} r_{\star}^k m_p c^2 (ct)^{3-k}} \right]^{1/2}, \quad (10)$$

with a radius evolving as (dot-dashed red line)

$$r_s(t) \approx \left(1 - \frac{1}{2(4-k)\Gamma_s^2(t)} \right) ct. \quad (11)$$

The main event ejecta (black) initially expand at constant speed into the cavity left behind by the precursor blastwave, and produce their gamma-ray emission (blue). The latter illuminates the blastwave when its radius is r_0 (see below). In our scenario, we assume this to happen later than the deceleration time. This corresponds to the condition $t_{\text{dec,obs}} < \Delta t_{\text{pre}}$, which implies a precursor ejecta bulk Lorentz factor $\Gamma_{\text{ej,pre}} \gtrsim 111 E_{\text{pre},52}^{1/8} n_{\text{ext},0}^{-1/8} \Delta t_{\text{pre},2.2}^{-3/8}$ for $k = 0$ or $\Gamma_{\text{ej,pre}} \gtrsim 26 E_{\text{pre},52}^{1/4} A_{\star,0}^{-1/4} \Delta t_{\text{pre},2.2}^{-1/4}$ for $k = 2$.

In the precursor blastwave, most of the shocked external medium material is confined within a thin shell of width $\Delta r_b \sim$

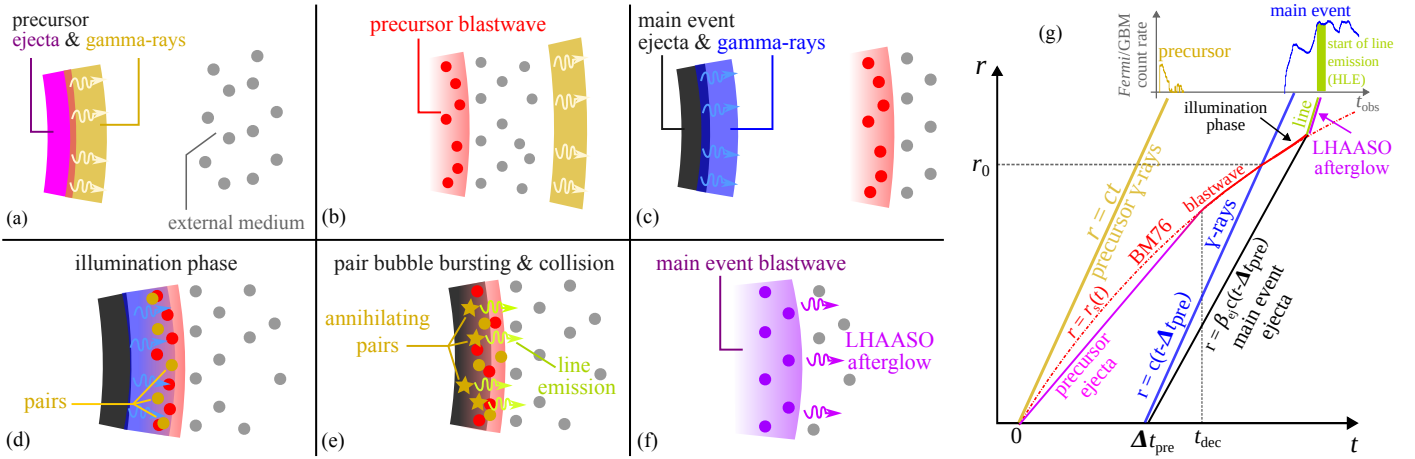


Fig. 3. Sketch of the proposed scenario (not to scale). After emitting their gamma-rays (a), the precursor ejecta expand into the external medium and drive a blastwave (b). The main event ejecta emit their gamma-rays (c) and initially expand in the cavity left by the precursor. The main event gamma-ray front illuminates the precursor blastwave (d) leading to copious pair creation and radiative acceleration. Soon after, the main event ejecta collide with the pair-enriched blastwave (e). The mass-annihilation of the pairs ('pair bubble bursting') happens somewhere between the end of (d) and the end of (e). When the main-event-ejecta-driven shock reaches the external medium, it leads to a much more energetic blastwave (f), whose emission (including the component seen by LHAASO) rises steeply before settling to the usual, self-similar evolution. Panel (g) shows the evolution of the radii of the components described in the other panels as a function of the 'lab-frame' time t in the progenitor rest frame. The inset shows the *Fermi*/GBM light curve, highlighting the connection between t and the observer-frame time t_{obs} .

r_s/Γ_s^2 behind the shock. Moreover, when the outer edge of the gamma-ray front is located at a radius r , the main event ejecta lag only shortly behind, at a distance $\Delta r_{\gamma,\text{ej}} \approx r/2\Gamma_{\text{ej}}^2 \lesssim \Delta r_b$, where Γ_{ej} is the main event ejecta bulk Lorentz factor. Hence, the interaction between the main event gamma-rays and the blastwave, before the main event ejecta catch up, happens entirely around the radius r_0 at which the gamma-ray front starts illuminating the blastwave shock. To compute this radius, let us consider a light pulse whose arrival time to the observer is delayed by Δt_{pre} with respect to the precursor emission. The radius of such pulse (blue line in panel g of Fig. 3) evolves simply as $r_\gamma = c(t - \Delta t_{\text{pre}})$. The gamma-ray front reaches the shock at a radius

$$r_0 \approx \left[\frac{(17 - 4k)(4 - k)E_{\text{pre}}c\Delta t_{\text{pre}}}{4\pi A_\star r_\star^k m_p c^2} \right]^{1/(4-k)}. \quad (12)$$

For the two external medium profiles of interest, we have

$$r_0 \approx \begin{cases} 3.6 \times 10^{16} E_{\text{pre},52}^{1/4} n_{\text{ext},2}^{-1/4} \Delta t_{\text{pre},2.2}^{1/4} \text{ cm,} & k = 0; \\ 1.3 \times 10^{16} E_{\text{pre},52}^{1/2} A_{\star,0}^{-1/2} \Delta t_{\text{pre},2.2}^{1/2} \text{ cm,} & k = 2. \end{cases} \quad (13)$$

In the $k = 0$ case, keeping the precursor ejecta kinetic energy fixed at the reference value, the external medium density must be at least $n_{\text{ext},2} \gtrsim 0.55 E_{\text{pre},52}^{-1}$ for r_0 to be in the range required by the HLE scenario (see Table 1), which explains why we take $n_{\text{ext}} = 10^2 \text{ cm}^{-3}$ as reference. An even larger n_{ext} in this case would also help in alleviating the extremely stringent requirement on the pair multiplicity (Eq. 8). In the $k = 2$ case, the density cannot be higher than $A_{\star,0} \approx 160 E_{\text{pre},52}^{-1}$, otherwise r_0 would become smaller than the minimum allowed value in the HLE scenario, $\sim 10^{15} \text{ cm}$.

From Eq. 10, the corresponding Lorentz factor of the material right behind the blastwave shock, $\Gamma_0 \sim \Gamma_s(r_0)/\sqrt{2}$, is

$$\Gamma_0 \approx \begin{cases} 22 E_{\text{pre},52}^{1/8} n_{\text{ext},2}^{-1/8} \Delta t_{\text{pre},2.2}^{-3/8}, & k = 0; \\ 18 E_{\text{pre},52}^{1/4} A_{\star,0}^{-1/4} \Delta t_{\text{pre},2.2}^{-1/4}, & k = 2. \end{cases} \quad (14)$$

By substituting r_0 back into the expressions for the Lorentz factor and pair multiplicity required in the HLE scenario, Eqs.

6 and 8, we can see how the HLE requirements depend on the blastwave parameters. For the Lorentz factor, we obtain

$$\Gamma_{\text{HLE}} \approx \begin{cases} 815 E_{\text{pre},52}^{1/4} n_{\text{ext},2}^{-1/4} \Delta t_{\text{pre},2.2}^{1/4} \left(\frac{t_{\text{line}} - t_0}{60 \text{ s}} \right)^{-1} \left(\frac{h\nu_{\text{line}}}{12.6 \text{ MeV}} \right)^{-1} & k = 0; \\ 276 E_{\text{pre},52}^{1/2} A_{\star,0}^{-1/2} \Delta t_{\text{pre},2.2}^{1/2} \left(\frac{t_{\text{line}} - t_0}{60 \text{ s}} \right)^{-1} \left(\frac{h\nu_{\text{line}}}{12.6 \text{ MeV}} \right)^{-1} & k = 2, \end{cases} \quad (15)$$

or

$$\frac{\Gamma_{\text{HLE}}}{\Gamma_0} \approx \begin{cases} 37 E_{\text{pre},52}^{1/8} n_{\text{ext},2}^{-1/8} \Delta t_{\text{pre},2.2}^{5/8} \left(\frac{t_{\text{line}} - t_0}{60 \text{ s}} \right)^{-1} \left(\frac{h\nu_{\text{line}}}{12.6 \text{ MeV}} \right)^{-1} & k = 0; \\ 15 E_{\text{pre},52}^{1/4} A_{\star,0}^{-1/4} \Delta t_{\text{pre},2.2}^{3/4} \left(\frac{t_{\text{line}} - t_0}{60 \text{ s}} \right)^{-1} \left(\frac{h\nu_{\text{line}}}{12.6 \text{ MeV}} \right)^{-1} & k = 2. \end{cases} \quad (16)$$

This shows that, along with pair-enrichment, some acceleration mechanism is needed in order to meet the required Lorentz factor. In Section 3.3 and in Appendix C we discuss two possible such mechanisms.

In the $k = 0$ case, we can express the pair multiplicity required in the HLE scenario, Eq. 8, as a function of the blastwave parameters, namely

$$Z_{\pm, \text{HLE}} - 1 \approx 6.5 \times 10^5 Y_e^{-1} E_{\text{pre},52}^{-1/2} n_{\text{ext},2}^{-1/2} \Delta t_{\text{pre},2.2}^{-1/2} L_{\text{line},50} \left(\frac{h\nu_{\text{line}}}{12.6 \text{ MeV}} \right)^{-3} \left(\frac{1+z}{1.15} \right)^{-3}. \quad (17)$$

The $k = 2$ case remains the same as in Eq. 8.

3.2. Energy in gamma-ray front and ejecta Lorentz factor

Let us indicate the energy in gamma-ray photons that flow through the blastwave during the illumination phase as $E_{\gamma f}$, and the associated average luminosity with L . In our scenario, the illumination phase ends at the time when the LHAASO light curve rises, that is around $t_{\text{obs}} \sim 226 \text{ s}$. Taking the results of the spectral analysis of Frederiks et al. (2023) in the time interval

$t_{\text{obs}} \in [180, 233]$ s as reference, we obtained $L \approx 4 \times 10^{52}$ erg s $^{-1}$ and $E_{\gamma f} \approx 1.6 \times 10^{54}$ erg. The fraction of this energy that needs to be converted into pairs to fulfil the requirement from Eq. 5 is

$$\frac{2\Gamma_{\text{HLE}}N_{\pm}m_{\text{e}}c^2}{E_{\gamma f}} \approx 0.4 r_{16}^2 L_{\text{line},50} \left(\frac{h\nu_{\text{line}}}{12.6 \text{ MeV}} \right)^{-4} \left(\frac{1+z}{1.15} \right)^{-3} \left(\frac{t_{\text{line}-t_0}}{60 \text{ s}} \right)^{-1} \quad (18)$$

This shows that the main event gamma-ray front contains in principle sufficient energy to produce the required pair loading, in presence of an efficient enough pair production mechanism.

As noted above, the radial extent of the gamma-ray front is $\Delta r_{\gamma, \text{ej}} \sim r_0/2\Gamma_{\text{ej}}^2$, and we have $E_{\gamma f}/L \sim \Delta r_{\gamma, \text{ej}}/c$. Therefore, the bulk Lorentz factor of the main event ejecta must have been

$$\Gamma_{\text{ej}} \approx 65 r_{0,16}^{1/2} \left(\frac{E_{\gamma f}/L}{40 \text{ s}} \right)^{-1/2} \quad (19)$$

in order for the assumptions behind our scenario to hold. At first sight, this low bulk Lorentz factor may seem in contradiction with that required by compactness arguments, $\Gamma_{\text{ej},0} \gtrsim 300 - 1000$ (Lesage et al. 2023; Gao & Zou 2023). However, we point out that (i) the collision involves at first the outermost part of the ejecta, which are associated with the first pulse of the main event (that extends approximately from 180 s to 210 s, Fig. 1). This pulse is less luminous and has a softer spectrum with respect to the most luminous peak, on which the Lesage et al. (2023) analysis is based; (ii) Γ_{ej} here refers to the bulk Lorentz factor of the ejecta long after the prompt emission, while the compactness limit applies to the bulk Lorentz factor $\Gamma_{\text{ej},0}$ of the ejecta in the act of producing such emission. In the case of a high prompt emission efficiency η_{γ} (which represents the fraction of the outflow energy that is radiated in gamma-rays), the radiation carries away sufficient energy and momentum to slow down significantly the ejecta. Indeed, energy and rest-mass conservation require $\Gamma_{\text{ej}} = (1 - \eta_{\gamma})\Gamma_{\text{ej},0}$. The limits from the compactness argument therefore do not conflict directly with our scenario, provided that a very high efficiency $\eta_{\gamma} = 1 - \Gamma_{\text{ej}}/\Gamma_{\text{ej},0} \sim 0.8 - 0.95$ could be realised in the main event gamma-ray emission, assuming $300 \lesssim \Gamma_{\text{ej},0} \lesssim 1000$ and $r_{0,16} = 1$. Conversely, a less extreme efficiency $\eta_{\gamma} = 0.5$, would lead to $\Gamma_{\text{ej},0} \approx 130 r_{0,16}^{1/2}$, which could be reasonable for the ejecta associated to the first pulse of the main event.

For what concerns the Lorentz factor estimates based on the assumption that the LHAASO peak corresponds to the deceleration time (LHAASO Collaboration et al. 2023; Lesage et al. 2023), we note that these neglect the presence of a precursor and its effect on the external medium, but rather arbitrarily shift the explosion time in order to match the initial rise power law slope expected in a scenario where the external medium has a uniform density. These estimates therefore cannot be compared to ours.

3.3. Requirements set by acceleration to the Lorentz factor implied by the HLE scenario

Two acceleration mechanisms operate on the blastwave after the start of the illumination phase: the momentum deposition by main event photons (radiative acceleration) and the subsequent hydrodynamical acceleration when the main event ejecta collide with the blastwave. As discussed later, we found that, for our source, only the former is relevant, hence we defer the discussion of the latter to Appendix C.

As discussed in Sect. 2.1, if the pair multiplicity reaches the required level, then the blastwave becomes a pair-dominated

shell (Eq. 8). Therefore, most of the rest mass is in pairs, $M_{\text{shell}} \sim 2N_{\pm}m_{\text{e}}$. If the shell is accelerated to the bulk Lorentz factor given in Eq. 6, its kinetic energy is roughly

$$\begin{aligned} \Gamma_{\text{HLE}}M_{\text{shell}}c^2 &\sim 2\Gamma_{\text{HLE}}N_{\pm}m_{\text{e}}c^2 \approx \\ &\approx 6.7 \times 10^{53} r_{16}^2 L_{\text{line},50} \left(\frac{h\nu_{\text{line}}}{12.6 \text{ MeV}} \right)^{-4} \left(\frac{1+z}{1.15} \right)^{-4} \left(\frac{t_{\text{line}} - t_0}{60 \text{ s}} \right)^{-1} \text{ erg.} \end{aligned} \quad (20)$$

For $r_{16} \lesssim 1.5$, we have $\Gamma_{\text{HLE}}M_{\text{shell}}c^2 \lesssim E_{\gamma f}$, therefore radiative acceleration could be efficient enough to meet the HLE requirement during the illumination phase.

3.4. Requirements set by pair cooling and annihilation

Pairs can cool due to inverse Compton (IC) scattering of main event photons, which, after the acceleration of the blastwave, happens mostly in the Thomson regime. The IC cooling time scale is $t'_{\text{cool}} \sim 3\pi m_{\text{e}}c^2 r^2 \Gamma^2 / \sigma_{\text{T}} L$, while the pair annihilation time (for cold pairs) is $t'_{\text{ann}} \sim 8/3\sigma_{\text{T}} c n_{\pm}'$. For the pair annihilation to produce a narrow line, the cooling time scale must be shorter than the annihilation time scale. Assuming again $V' = 4\pi\xi r^3/\Gamma$ (see Section 2.1) and substituting N_{\pm} from Eq. 5 and Γ from Eq. 6, we obtain

$$\frac{t'_{\text{ann}}}{t'_{\text{cool}}} \approx 0.3 r_{16}^{-3} \xi_{-1} L_{52.6} L_{\text{line},50}^{-1} \left(\frac{h\nu_{\text{line}}}{12.6 \text{ MeV}} \right)^6 \left(\frac{1+z}{1.15} \right)^3 \left(\frac{t_{\text{line}} - t_0}{60 \text{ s}} \right)^3. \quad (21)$$

Therefore, pairs cool faster than they annihilate as long as

$$r_{16} \lesssim 0.7 \xi_{-1}^{1/3} L_{52.6}^{1/3} L_{\text{line},50}^{-1/3} \left(\frac{h\nu_{\text{line}}}{12.6 \text{ MeV}} \right)^2 \left(\frac{1+z}{1.15} \right) \left(\frac{t_{\text{line}} - t_0}{60 \text{ s}} \right). \quad (22)$$

These calculations show that, within a sizable fraction of the parameter space allowed by the HLE scenario, the pairs are expected to cool efficiently (and hence produce a narrow annihilation line) and to annihilate fast enough for the HLE effect to dominate the observed line evolution.

4. The illumination phase: pair enrichment and radiative acceleration

4.1. Non-thermal electrons in the blastwave

In order to work out the effect of the main event photons on the blastwave, we need to describe the leptonic content of the latter. We assume electrons from the external medium to be accelerated at the blastwave shock, with an injection rate distributed as a power law in the electron Lorentz factor, $dn'_{\text{e,inj}}/dy \propto y^{-p}$, and we fix the power law index at $p = 2.2$ based on the results of particle-in-cell simulations of relativistic shocks in weakly magnetized media (Sironi et al. 2013). After leaving the acceleration region, electrons keep interacting with the shock-generated, turbulent magnetic field, producing synchrotron emission. Electrons can also interact with synchrotron photons, producing synchrotron-self Compton (SSC) emission. These emission processes affect the electron energy distribution across the blastwave.

We adopt here a simplified description of the blastwave structure as a homogeneous shell whose density is given by the ultra-relativistic Rankine-Hugoniot condition $n \sim 4\Gamma_0\Gamma_0 n_{\text{ext}}(r_0)$.

Conservation of the external medium rest mass then implies an effective shell thickness $\Delta r_0 = r_0/4(3 - k)\Gamma_0^2$.

Assuming the acceleration process to affect a fraction $\xi_N \sim 1$ of the external medium electrons, and defining $\epsilon_e = 0.1\epsilon_{e,-1}$ as the fraction of the shock downstream internal energy that is shared by the accelerated electrons, we have that the minimum Lorentz factor of injected electrons is $\gamma_m \sim (p - 2)\epsilon_e\Gamma_0 m_p/(p - 1)m_e$, which gives

$$\gamma_m \approx \begin{cases} 670\epsilon_{e,-1}E_{\text{pre},52}^{1/8}n_{\text{ext},2}^{-1/8}\Delta t_{\text{pre},2,2}^{-3/8}, & k = 0; \\ 550\epsilon_{e,-1}E_{\text{pre},52}^{1/4}A_{\star,0}^{-1/4}\Delta t_{\text{pre},2,2}^{-1/4}, & k = 2. \end{cases} \quad (23)$$

Most of the electrons contained in the shell were accelerated during the last dynamical time $t'_\text{dyn} = r_0/(\Gamma_0 c)$. Over that time, electrons accelerated to an initial Lorentz factor larger than γ_c had time to lose most of their energy by synchrotron and synchrotron-self-Compton radiation, with

$$\gamma_c \sim \frac{6\pi m_e c^2 \Gamma_0}{\sigma_T r_0 B'^2 (1 + Y')} \equiv \frac{\gamma_{c,\text{syn}}}{1 + Y'}, \quad (24)$$

where σ_T is the Thomson cross section, B' is the average strength of the turbulent magnetic field in the shock downstream, Y' is the ‘Compton parameter’, that is, the ratio of the SSC to the synchrotron losses for electrons with $\gamma = \gamma_c$. Assuming the turbulent magnetic field to share a fraction $\epsilon_B = 10^{-3}\epsilon_{B,-3}$ of the shock downstream internal energy, we have $B' = \sqrt{32\pi\epsilon_B\Gamma_0^2 n_{\text{ext}}(r_0)m_p c^2}$. For our early time of interest, we find that SSC cooling dominates over synchrotron, with (see Eq. 35 in Panaiteescu & Kumar 2000)

$$1 + Y' = \frac{1}{2} \left[-1 + \sqrt{\frac{(5 - k)\epsilon_e}{2(3 - k)\epsilon_B} + 1} \right] \approx \begin{cases} 4.1\epsilon_{e,-1}^{1/2}\epsilon_{B,-3}^{-1/2} & k = 0; \\ 5.6\epsilon_{e,-1}^{1/2}\epsilon_{B,-3}^{-1/2} & k = 2, \end{cases} \quad (25)$$

which then gives

$$\gamma_c \sim \begin{cases} 480\epsilon_{e,-1}^{-1/2}\epsilon_{B,-3}^{-1/2}n_{\text{ext},2}^{-5/8}E_{\text{pre},52}^{-3/8}\Delta t_{\text{pre},2,2}^{1/8}, & k = 0; \\ 62\epsilon_{e,-1}^{-1/2}\epsilon_{B,-3}^{-1/2}A_{\star,0}^{-5/4}E_{\text{pre},52}^{1/4}\Delta t_{\text{pre},2,2}^{3/4}, & k = 2. \end{cases} \quad (26)$$

As a result of acceleration and cooling, the Lorentz factor distribution of the electrons in the blastwave approximately follows a broken power law, which can be summarised as

$$\frac{dn'_e}{d\gamma} \sim \frac{n'_e}{\gamma_c} \begin{cases} \left(\frac{\gamma}{\gamma_c}\right)^{-2} & \gamma_c \leq \gamma < \gamma_m \\ \left(\frac{\gamma_m}{\gamma_c}\right)^{-2} \left(\frac{\gamma}{\gamma_m}\right)^{-p-1} & \gamma_m \leq \gamma \\ 0 & \text{otherwise} \end{cases}, \quad (27)$$

which shows that most electrons in the blastwave have a Lorentz factor close to γ_c .

4.2. Incident main event spectrum and inverse Compton cooling of the blastwave original electrons

As soon as the blastwave is illuminated by the main event photons, these can be subject to inverse Compton scattering off the blastwave electrons. Let ε be a main event photon energy in units of the electron rest mass energy, and let L_ε be the specific luminosity of the main event emission per unit of ε . The spectrum of the latter can be described as

$$L_\varepsilon = \frac{L}{\varepsilon_{\text{peak}}} f_{\text{main}} \left(\frac{\varepsilon}{\varepsilon_{\text{peak}}} \right), \quad (28)$$

where we defined the main event spectral shape following the empirical ‘Band’ function (Band et al. 1993)

$$f_{\text{main}}(x) \propto \begin{cases} x^{1-\alpha_1} e^{-(2-\alpha_1)x} & x \leq \frac{(\alpha_2-\alpha_1)}{(2-\alpha_1)} \\ x^{1-\alpha_2} \left(\frac{\alpha_2-\alpha_1}{2-\alpha_1}\right)^{\alpha_2-\alpha_1} e^{\alpha_1-\alpha_2} & \frac{(\alpha_2-\alpha_1)}{(2-\alpha_1)} < x \leq x_{\text{cut}} \\ 0 & x > x_{\text{cut}} \end{cases}, \quad (29)$$

with $x = \varepsilon/\varepsilon_{\text{peak}}$.

As per the spectral analysis reported in Frederiks et al. (2023), the average spectrum of the main event has $\alpha_1 \approx 0.89$, $\alpha_2 \approx 2.21$ and $E_{\text{peak}} \approx 2660$ keV, which translates into $\varepsilon_{\text{peak}} = (1+z)E_{\text{peak}}/m_e c^2 \approx 6$. As noted in Section 3.2, during our period of interest, using the results from the analysis in the same paper, we have $L \approx 4 \times 10^{52}$ erg s⁻¹ (integrated in the 20 keV – 10 MeV band). The normalization of f_{main} is set so that

$$\int_{(1+z)20\text{ keV}/\varepsilon_{\text{peak}}}^{(1+z)10\text{ MeV}/\varepsilon_{\text{peak}}} f_{\text{main}}(x) dx = 1. \quad (30)$$

In the spectral shape, we introduced a high-energy cut-off at an observed photon energy $E_{\text{cut}} = x_{\text{cut}}\varepsilon_{\text{peak}}m_e c^2/(1+z)$ (discussed later).

The typical electron in the blastwave sees the incident spectral luminosity peak at $\varepsilon'' \sim \gamma_c \varepsilon_{\text{peak}}/\Gamma_0$. The IC scattering of photons at that peak is in the Thomson regime provided that $\varepsilon'' \lesssim 1$, which is verified as long as

$$\begin{aligned} n_{\text{ext}} &\gtrsim 1.7 \times 10^6 \epsilon_{e,-1}^{-1} \epsilon_{B,-3}^{-1} E_{\text{pre},52}^{-1} \Delta t_{\text{pre},2,2} \text{ cm}^{-3}, & k = 0; \\ A_\star &\gtrsim 21 \epsilon_{e,-1}^{-1/2} \epsilon_{B,-3}^{-1/2} \Delta t_{\text{pre},2,2}^{-3} \text{ cm}^{-3}, & k = 2. \end{aligned} \quad (31)$$

In the following, we will demonstrate that these conditions are always satisfied in the regions of interest of our parameter space. In the Thomson regime, the IC cooling time scale is

$$t'_{\text{cool}} \sim \begin{cases} 180 L_{52,6}^{-1} E_{\text{pre},52}^{3/4} n_{\text{ext},2}^{-3/4} \Delta t_{\text{pre},2,2}^{-1/4} \text{ s}, & k = 0; \\ 14 L_{52,6}^{-1} E_{\text{pre},52}^{3/2} A_{\star,0}^{-3/2} \Delta t_{\text{pre},2,2}^{1/2} \text{ s}, & k = 2. \end{cases} \quad (32)$$

This is shorter than the illumination phase duration, $t'_{\text{cool}} \ll \Delta t'_{\text{ill}}$, with

$$\Delta t'_{\text{ill}} \gtrsim \Gamma_0 E_{\gamma f}/L \approx \left(\frac{E_{\gamma f}/L}{40 \text{ s}} \right) \begin{cases} 870 E_{\text{pre},52}^{1/8} n_{\text{ext},2}^{-1/8} \Delta t_{\text{pre},2,2}^{-3/8} \text{ s} & k = 0; \\ 720 E_{\text{pre},52}^{1/4} A_{\star,0}^{-1/4} \Delta t_{\text{pre},2,2}^{1/4} \text{ s} & k = 2, \end{cases} \quad (33)$$

provided that

$$\begin{aligned} n_{\text{ext}} &\gg 8 E_{\gamma f,54,2}^{-8/5} E_{\text{pre},52} \Delta t_{\text{pre},2,2}^{1/5} \text{ cm}^{-3}, & k = 0; \\ A_\star &\gg 0.04 E_{\gamma f,54,2}^{-4/5} E_{\text{pre},52} \Delta t_{\text{pre},2,2}^{3/5} \text{ cm}^{-3}, & k = 2, \end{aligned} \quad (34)$$

which is also always verified in our parameter space of interest. We conclude that we can consider the electrons (and any generated pairs) as cold during the illumination phase. This greatly simplifies the computation of the pair enrichment and radiative acceleration.

4.3. Description of pair enrichment and acceleration

The basic process that leads to pair production and radiative acceleration in the illumination phase is sketched in Fig. 4 and consists of two steps: (i) an incident photon is Compton-scattered off a lepton and (ii) another incident photon annihilates with it, forming an electron-positron pair. Because the blastwave is

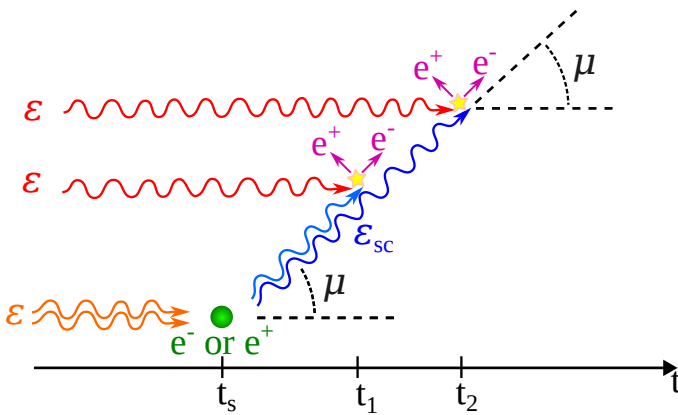


Fig. 4. Fundamental block of the process that leads to e^+e^- pair enrichment and acceleration within the blastwave. A packet of incident photons with energy ε (orange) is inverse-Compton scattered at time t_s by an electron or positron (green) into a packet of photons with energy ε_{sc} (blue) that propagates with a cosine angle $\cos \theta = \mu$ with respect to the incident photon direction. Subsequent interactions of the scattered photons with incident photons of typical energy $\varepsilon \sim \varepsilon_{th} = 2/(1 - \mu)\varepsilon_{sc}$ (red) lead to pair production (two example such interactions happening at times t_1 and t_2 are shown in the sketch), gradually suppressing the scattered photon packet intensity by a factor $\exp[-c(t - t_s)/\lambda_{\gamma\gamma}(\varepsilon_{sc}, \mu)]$, where $\lambda_{\gamma\gamma}$ is the mean free path of the interaction.

magnetized, all leptons remain tied to the local plasma. As a result, given that the incident photons are almost perfectly radial, both the scattering and the pair production deposit momentum in the plasma, which is therefore accelerated by the process. The pairs contribute to the optical depth of the medium, enhancing the probability of further scattering of incident photons and consequent pair production. The acceleration, on the other hand, reduces the incident luminosity and redshifts the incident photon spectrum in the comoving frame, working against the former effects. We describe the scattering, pair production and plasma acceleration following a similar treatment as [Beloborodov \(2002\)](#), hereafter [Be02](#). In Appendix D we give a complete derivation (which allowed us to identify some misprints in the original paper) and technical details about our implementation. Here we mention the fact that we included the feedback of pair annihilation in both the pair production rate and in the acceleration, differently from [Be02](#).

The initial conditions of the calculation are the precursor blastwave parameters, $(A_\star, E_{\text{pre}})$ or $(n_{\text{ext}}, E_{\text{pre}})$, the electron fraction Y_e of the external medium, and the incident spectrum. For the latter, we use the spectral parameters from Section 4.2. The cut-off photon energy E_{cut} remains to be specified. Given a set of parameters $(A_\star, E_{\text{pre}}, Y_e, E_{\text{cut}})$, the calculation yields the pair multiplicity, the pair-enriched blastwave Lorentz factor and the number of annihilated pairs as a function of time, or equivalently of $E_{\gamma f}$ (to be understood here as the energy in the incident radiation that flowed through the blastwave until a given time during the illumination phase), $Z_\pm(E_{\gamma f})$, $\Gamma_1(E_{\gamma f})$ and $N_{\pm, \text{ann}}(E_{\gamma f})$. As discussed in Section 3.2, we assume that the illumination phase ends at $E_{\gamma f} = 1.6 \times 10^{54}$ erg, which corresponds to the main event energy before the steep rise of the LHAASO afterglow.

As we show below, the required pair enrichment can only be reached in presence of a very high external density, which could be linked to enhanced progenitor star mass loss during the late stages of its evolution, as discussed later. The expected electron fraction in such a scenario is $Y_e = 0.5$, and we kept it set to that value (choosing $Y_e = 1$ has a minor impact on our results).

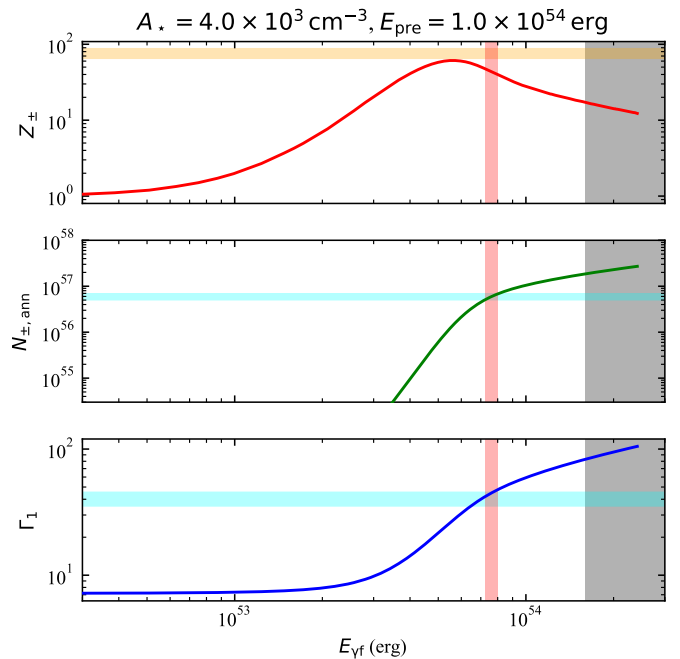


Fig. 5. Example illumination phase evolution of pair enrichment and radiative acceleration. The three panels show the evolution of the pair multiplicity (Z_\pm , top panel), number of annihilated pairs ($N_{\pm, \text{ann}}$, middle panel) and bulk Lorentz factor (Γ_1 , bottom panel) as a function of time or equivalently of $E_{\gamma f}$ (i.e. the total energy in the incident radiation until a given time) for a blastwave in an external medium with $k = 2$, with density parameter $A_\star = 4 \times 10^3 \text{ cm}^{-3}$ and with a precursor blastwave energy $E_{\text{pre}} = 10^{54}$ erg, corresponding to an illumination radius $r_0 \approx 2.1 \times 10^{15}$ cm. The grey shaded area corresponds to times after the main event ejecta collided with the blastwave. The vertical red band shows the range of $E_{\gamma f}$ for which the number of annihilated pairs satisfy the constraints imposed by the HLE interpretation. The horizontal bands show the pair multiplicity (top panel), number of annihilated pairs (middle panel) and bulk Lorentz factor (bottom panel), respectively, required by the HLE interpretation if the annihilation takes place at r_0 .

For what concerns E_{cut} , we found its impact to be very limited unless $E_{\text{cut}} \lesssim 10$ MeV, in which case both the enrichment and the radiative acceleration are strongly suppressed. We thus fixed $E_{\text{cut}} = 100$ MeV.

Figure 5 shows an example evolution, which corresponds to $k = 2$ and $(A_\star, E_{\text{pre}}) = (4 \times 10^3 \text{ cm}^{-3}, 10^{54} \text{ erg})$. The figure demonstrates that, for these initial parameters, a sufficient number of produced pairs annihilate when the blastwave has the required bulk Lorentz factor.

4.4. Results

When varying the initial conditions, we found two possible types of Z_\pm evolution during the illumination phase: either the pair multiplicity peaks and then decreases at some point before the end of the illumination phase (such as in Fig. 5), or it increases monotonically. This corresponds to two possible regimes: in the former, the pair density reaches a critical value beyond which the annihilation rate surpasses the pair creation rate, leading to a mass-annihilation during the illumination phase; in the latter, no such mass annihilation takes place, but it can still be triggered by the main event ejecta collision later, as discussed in Appendix C. From our numerical results, we found that all cases which can satisfy the constraints imposed by the HLE interpre-

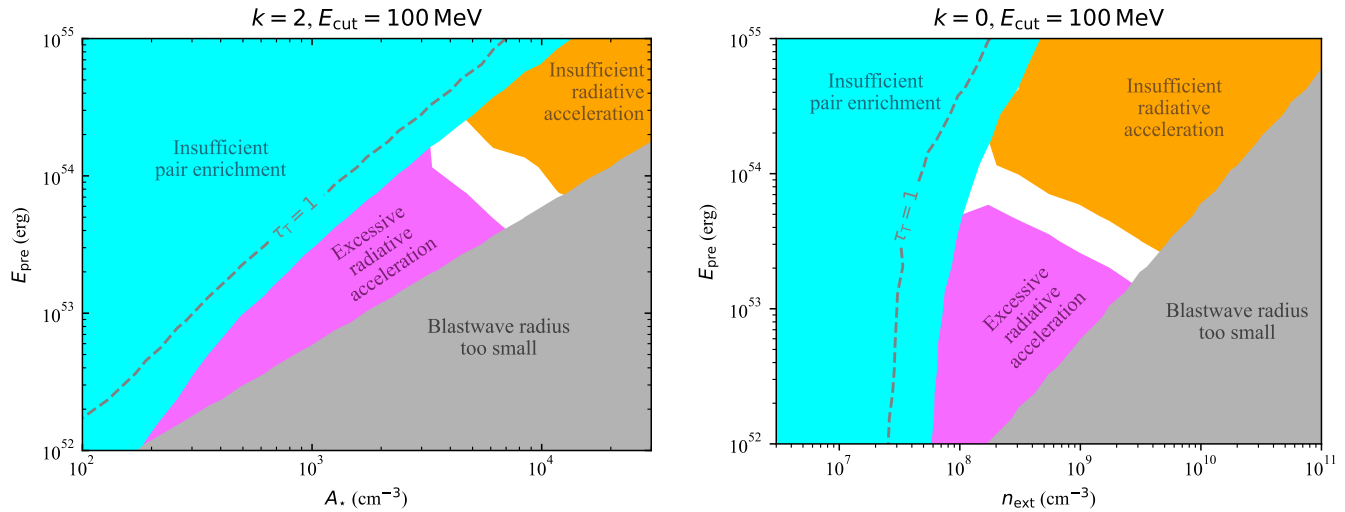


Fig. 6. Precursor blastwave parameter space constraints assuming $E_{\text{cut}} = 100$ MeV. Coloured regions in the figures show regions on the (A_*, E_{pre}) plane ($k = 2$, left-hand panel) or $(n_{\text{ext}}, E_{\text{pre}})$ plane ($k = 0$, right-hand panel) where the following constraints imposed by the HLE interpretation (see Sect. 2.1.2) are violated during the illumination phase: the blastwave radius is smaller than 10^{15} cm ($r_{0,16} < 0.1$, grey); an insufficient number of annihilating pairs are produced ($N_{\pm,\text{ann},57}/r_{0,16} < 2.5$, cyan); the radiative acceleration before the pair mass-annihilation is too efficient ($\Gamma_1/r_{0,16} > 220$ when $N_{\pm,\text{ann},57}/r_{0,16} = 2.5$, magenta); the radiative acceleration is insufficient ($\Gamma_1/r_{0,16} < 173$ when $N_{\pm,\text{ann},57}/r_{0,16} = 3.3$, orange). In the region to the right of the dashed line, the blastwave becomes optically thick to Thomson scattering during the illumination phase.

tation are cases where the mass-annihilation takes place during the illumination phase.

From the analysis described in Section 2.1.2, we found that the number of annihilating pairs should satisfy $2.5 < N_{\pm,\text{ann},57}/r_{0,16} < 3.3$ (union of the 90% credible intervals of the two analyses discussed there). If this condition was satisfied for some initial conditions, we then checked whether $173 < \Gamma_1/r_{0,16} < 220$ during the same phase. Figure 6 shows the constraints imposed by these conditions on the (A_*, E_{pre}) or $(n_{\text{ext}}, E_{\text{pre}})$ plane. The cyan region marks initial conditions for which $N_{\pm,\text{ann},57}/r_{0,16} < 2.5$ at all times, hence not enough annihilating pairs are produced; the magenta region shows points where enough pairs are produced, but the blastwave Lorentz factor is too high when this happens; similarly, the orange region shows cases for which the blastwave is too slow when the mass-annihilation takes place. The grey region additionally shows cases for which $r_{0,16} < 0.1$, that is, the blastwave radius is too small. In the figure we also show a grey dashed line, which marks the initial conditions to the right of which the blastwave becomes optically thick to Thomson scattering at some point during the illumination phase. This happens consistently when the pair production satisfies our constraints.

5. Discussion

For both the $k = 0$ and $k = 2$ cases, a (quite narrow) region in our parameter space exists where all constraints are satisfied. This corresponds to $10^8 \lesssim n_{\text{ext}}/\text{cm}^{-3} \lesssim 10^9$ and $2 \times 10^{53} \lesssim E_{\text{pre}}/\text{erg} \lesssim 10^{54}$ for $k = 0$, or $3 \times 10^3 \lesssim A_*/\text{cm}^{-3} \lesssim 10^4$ and $4 \times 10^{53} \lesssim E_{\text{pre}}/\text{erg} \lesssim 3 \times 10^{54}$ for $k = 2$. Qualitatively, these conditions correspond to a very low prompt emission efficiency of the precursor (of about 0.1–1 percent) and a very high external density, which in both cases is 10^8 – 10^9 cm $^{-3}$ at the distance where the pair-loading takes place. Here we discuss our interpretation of these outcomes.

5.1. Interpretation of the high required external density

The high external density could be due to a dense circumstellar medium (CSM) in the close vicinity of the progenitor (our results only require the high density region to extend out to $r_0 \sim \text{few} \times 10^{15}$ cm). This could be realised if the stellar wind of the progenitor massive star was enhanced during the last few years before the supernova explosion. This scenario is best described assuming $k = 2$. Calling \dot{M}_w the progenitor mass-loss rate and v_w the typical velocity of the progenitor winds, we have

$$A_* = \frac{\dot{M}_w}{4\pi v_w r_*^2 m_p} \approx 10^3 \left(\frac{\dot{M}_w}{10^{-2} M_\odot \text{yr}^{-1}} \right) \left(\frac{v_w}{10^3 \text{km s}^{-1}} \right)^{-1}. \quad (35)$$

Calling $T \approx 1 T_{7.5}$ yr the duration of the eruptive phase, the extent of the high-density circumstellar medium around the progenitor star is $R \sim v_w T \approx 3 \times 10^{15} v_{w,8} T_{7.5}$ cm, which easily accommodates the condition $r_0 \lesssim R$.

If the enhanced mass loss phase was interrupted some years before the explosion, pressure waves may have had the time to smooth out the external density gradients, resulting in a more homogeneous medium, perhaps better described by $k = 0$. In this case, a density $n_{\text{ext}} = 10^8 n_{\text{ext},8} \text{cm}^{-3}$ implies a mass enclosed within $R = 3 \times 10^{15} R_{15.5}$ cm of $M \sim m_p n_{\text{ext}} 4\pi R^3/3 \approx 10^{-2} n_{\text{ext},8} R_{15.5}^3 M_\odot$. Hence both the $k = 0$ and $k = 2$ cases require a similar, very intense progenitor mass loss in the final years before the final explosion.

Evidence of circumstellar media with densities as high as, or even higher than, those found here have been invoked to explain narrow-line core-collapse supernovae (Type IIn SNe, Schlegel 1990) such as SN1994W (Chugai et al. 2004). The origin could be eruptive mass ejection in a luminous-blue-variable (LBV) phase of the progenitor taking place in the final stages of the stellar evolution (Kiewe et al. 2012). An intriguing alternative proposed by Chevalier (2012) is a scenario where the progenitor is a binary involving a compact object and a red supergiant that undergo a common envelope phase. By moving through the

common envelope, the compact object ejects a large amount of matter, giving birth to the dense CSM. The common envelope phase could end with the compact object merging with the core of the companion, resulting in a short-lived Thorne-Zytkow object (Thorne & Zytkow 1977) that eventually explodes.

Optical and infrared observations (Fulton et al. 2023; Levan et al. 2023; Srinivasaragavan et al. 2023; Blanchard et al. 2024; Kong et al. 2024) revealed supernova (SN) emission associated with this GRB, with a luminosity slightly lower than that of the prototypical SN1998bw (Galama et al. 1998) and in line with other GRB-associated SNe. This may suggest that, whatever the nature of the progenitor of the peculiar GRB studied here, this should not be vastly different from those of other GRBs with an associated SN, and hence the presence of a CSM could be a common feature of GRB progenitors, rather than a distinctive property of GRB 221009A.

5.2. Interpretation of the low precursor gamma-ray efficiency

The low gamma-ray efficiency of the precursor contrasts with the very high efficiency of the main event suggested by the main event ejecta Lorentz factor constraint (Sect. 3.2). A dense CSM, on the other hand, could have acted as a ‘Thomson screen’, letting out only a fraction $e^{-\tau_{\text{CSM}}}$ of the precursor radiation, where τ_{CSM} is the CSM optical depth. Under this assumption, we can obtain some instructive constraints on either the outer radius R_{CSM} of the CSM (if $k = 2$) or the radius r_γ of the prompt emission (if $k = 0$). In general, the Thomson optical depth of the CSM, for photons emitted at a radius r_γ , is given by

$$\tau_{\text{CSM}} \sim \sigma_{\text{T}} \int_{r_\gamma}^{R_{\text{CSM}}} n_{\text{ext}}(r) dr = \frac{\sigma_{\text{T}} A_\star r_\star}{1-k} \left[\left(\frac{R_{\text{CSM}}}{r_\star} \right)^{1-k} - \left(\frac{r_\gamma}{r_\star} \right)^{1-k} \right]. \quad (36)$$

If we require the precursor gamma-ray isotropic-equivalent energy $E_{\gamma,\text{pre}} \sim 10^{51}$ erg to be equal to $e^{-\tau_{\text{CSM}}} \eta_{\gamma,\text{pre}} E_{\text{pre}}$, we have

$$\tau_{\text{CSM}} \sim \ln \left(\frac{\eta_{\gamma,\text{pre}} E_{\text{pre}}}{E_{\gamma,\text{pre}}} \right) \approx 4.6, \quad (37)$$

where the numerical value assumes $E_{\text{pre}} = 10^{54}$ erg and $\eta_{\gamma,\text{pre}} = 0.1$. For $k = 2$, assuming $R_{\text{CSM}} \gg r_\gamma$, we obtain

$$\begin{aligned} r_\gamma &\sim \frac{\sigma_{\text{T}} A_\star r_\star^2}{\ln(\eta_{\gamma,\text{pre}} E_{\text{pre}} / E_{\gamma,\text{pre}})} \approx \\ &\approx 1.7 \times 10^{14} A_{\star,3.6} \left[\frac{\ln(\eta_{\gamma,\text{pre}} E_{\text{pre}} / E_{\gamma,\text{pre}})}{4.6} \right]^{-1} \text{ cm}. \end{aligned} \quad (38)$$

Conversely, if $k = 0$, we obtain a constraint on the CSM radius, which reads

$$\begin{aligned} R_{\text{CSM}} &\sim \frac{\ln(\eta_{\gamma,\text{pre}} E_{\text{pre}} / E_{\gamma,\text{pre}})}{\sigma_{\text{T}} n_{\text{ext}}} \approx \\ &\approx 7 \times 10^{15} n_{\text{ext},0} \left[\frac{\ln(\eta_{\gamma,\text{pre}} E_{\text{pre}} / E_{\gamma,\text{pre}})}{4.6} \right] \text{ cm}. \end{aligned} \quad (39)$$

Both constraints suggest that the efficiency of the precursor emission could have been ‘ordinary’, but that the observed radiation only consisted of the small fraction of photons that avoided Thomson scattering within the CSM. We give a more detailed account of the effect of a dense CSM on the observed spectrum of the prompt emission in Oganesyan et al. (in preparation).

5.3. Caveat about the Thomson optical depth of the pair-enriched blastwave

Our calculation of the pair enrichment and acceleration assumes that incident photons undergo only one Compton scattering before annihilating with other incident photons. If the Thomson optical depth of the blastwave becomes larger than unity, multiple scatterings become probable. Intuitively, we expect multiple scatterings to enhance the pair production efficiency beyond what is predicted by our model, because of an enhanced probability of more favourable angles for photon-photon collisions. It is therefore possible that a more advanced calculation could reduce the external density requirements. Nevertheless, because the $\tau_{\text{T}} = 1$ lines in Fig. 6 are only slightly to the left of the allowed regions we found with our current treatment, we expect the impact of such a more advanced calculation not to change qualitatively the conclusions of this work.

5.4. Non-thermal emission by pairs before their annihilation

Pairs produced during the illumination phase are born mildly relativistic, with $\gamma_\pm \sim 10$ ((Be02)), before cooling over a time scale t'_{cool} . The cooling is dominated by IC: the synchrotron emission over the same time scale is comparatively much weaker, as can be seen by taking the ratio of the radiation energy density at the start of the illumination phase $u'_{\text{rad}} = L/4\pi r_0^2 \Gamma_0^2 c$ to the magnetic energy density in the blastwave, $u'_{\text{B}} = B^2/8\pi$, which gives, for both $k = 0$ and $k = 2$,

$$\frac{u'_{\text{rad}}}{u'_{\text{B}}} \approx 0.23 \frac{\Delta t_{\text{pre}} L}{E_{\text{pre}} \epsilon_{\text{B}}} \approx 1.4 \times 10^3 \Delta t_{\text{pre},2.2} L_{52.6} \epsilon_{\text{B},-3}^{-1} E_{\text{pre},54}^{-1}. \quad (40)$$

The energy released in IC by each pair in the shell comoving frame is simply $2(\gamma_\pm - 1)m_e c^2$. Because the process happens on the same time scale as the mass-annihilation, the luminosity is set by the HLE effect and is therefore approximately equal to the total energy emitted, $E_{\gamma,\text{IC}} \sim 2(\gamma_\pm - 1)\Gamma_{\text{HLE}} N_\pm m_e c^2$, divided by the angular time scale $t_{\text{ang}} \sim \frac{r_0}{2\Gamma_{\text{HLE}}^2 c}$. This yields an IC luminosity of the cooling pairs of about

$$\begin{aligned} L_{\gamma,\text{IC}} &\approx \left(\frac{\gamma_\pm - 1}{10} \right) L_{\text{line},50} \left(\frac{t_{\text{line}} - t_0}{60 \text{ s}} \right)^{-3} \left(\frac{h\nu_{\text{line}}}{12.6 \text{ MeV}} \right)^{-6} \left(\frac{1+z}{1.15} \right)^{-3} \times \\ &\times \begin{cases} 9 \times 10^{50} \Delta t_{\text{pre},2.2}^{3/4} E_{\text{pre},54}^{3/4} n_{\text{ext},9}^{-3/4} \text{ erg s}^{-1} & k = 0; \\ 4 \times 10^{51} \Delta t_{\text{pre},2.2}^{3/2} E_{\text{pre},54}^{3/2} A_{\star,4}^{-3/2} \text{ erg s}^{-1} & k = 2. \end{cases} \end{aligned} \quad (41)$$

This IC spectrum peaks at around $\gamma_\pm^2 \epsilon_{\text{peak}} m_e c^2 \approx 260 \gamma_{\pm,1}^2 (\epsilon_{\text{peak}}/6) \text{ MeV}$ and would therefore fall into *Fermi*’s Large Area Telescope (*Fermi*/LAT) band. Intriguingly, emission with a luminosity of a few 10^{51} erg s $^{-1}$ was seen in *Fermi*/LAT, starting at the same time as the LHAASO afterglow (Axelsson et al. 2025, see e.g. their figure 9). Whether this emission contains a contribution from the kind of process described here, in addition to the afterglow, is hard to assess, but could be worth a detailed investigation.

5.5. Similar line emission in other GRBs

An important question is whether a similar line emission process is to be expected in other GRBs, and in which circumstances.

The process described here requires a high external density. As demonstrated in this work, even with as favourable a spectrum as that of GRB 221009A, the requirement is $A_\star \gtrsim 10^3 \text{ cm}^{-3}$ (we focus hereafter on $k = 2$ for simplicity).

The precursor is also a key ingredient: if a cavity within the high-density environment were not present, the illumination phase would be very brief, because the ejecta would collide immediately with the external medium, accelerating it and hence reducing the incident photon energies in the external medium comoving frame. The condition $r_0 \gg r_\gamma$ imposes a stringent requirement on the precursor energy and on the duration of the quiescence that separates it from the main event phase, which reads

$$E_{\text{pre}} \Delta t_{\text{pre}} \gg 10^{54} A_{\star,4} r_{\gamma,14}^2 \text{ erg s.} \quad (42)$$

If we assume a low gamma-ray efficiency for the precursor, $\eta_{\gamma,\text{pre}} = 10^{-3} \eta_{\gamma,\text{pre,-3}}$ (for the reasons discussed in Section 5.2), this can be written as

$$E_{\gamma,\text{pre}} \Delta t_{\text{pre}} \gg 10^{51} A_{\star,4} r_{\gamma,14}^2 \eta_{\gamma,\text{pre,-3}} \text{ erg s.} \quad (43)$$

At the beginning of the illumination phase, the blastwave must have decelerated to a low enough Lorentz factor so that a large fraction of the main event spectrum is above the pair production threshold. This can be translated into the requirement $(1+z)E_{\text{peak}}/\Gamma_0 \gtrsim m_e c^2$, or $\varepsilon_{\text{peak}} \gtrsim \Gamma_0$. This imposes a stringent requirement on the separation between precursor and main event, namely

$$\Delta t_{\text{pre}} \gtrsim 160 \varepsilon_{\text{peak},0.5}^4 E_{\gamma,\text{pre},50} \eta_{\gamma,\text{pre,-3}} A_{\star,4} \text{ s.} \quad (44)$$

This indicates that the most favourable conditions for finding a similar line in other GRBs are the presence of a long quiescence followed by luminous emission with a very hard spectrum.

6. Summary and conclusions

In this paper, we showed that the narrow emission line at around 10 MeV found in GRB221009A spectra by [Ravasio et al. \(2024\)](#) can be successfully interpreted as high-latitude emission from a thin shell of annihilating e^-e^+ pairs, provided that the shell radius, Lorentz factor and pair number satisfy specific constraints. We conceived a scenario that can produce a pair-loaded shell with the required properties: before being loaded with pairs, the shell is the blastwave produced by the ejecta of the GRB221009A precursor when expanding into a dense circumstellar medium. When the blastwave is located at a radius $r_0 \sim \text{few} \times 10^{15} \text{ cm}$, and it is still expanding with a bulk Lorentz factor of $\Gamma_0 \sim \text{few}$, it is illuminated by the bright main event in the GRB prompt emission. Incident photons are scattered within the blastwave and annihilate with other incident photons to produce e^-e^+ pairs, which end up being two orders of magnitude more abundant than the original electrons in the blastwave. Momentum deposition by scattering and pair creation accelerates and compresses the blastwave, until the pairs mass-annihilate, producing the line. Because the mass-annihilation happens over a time interval much smaller than r_0/c , the observed evolution of the line is dominated by the high-latitude effect. Soon after the mass-annihilation, the main event ejecta catch up and collide with the blastwave and ultimately with the unperturbed external medium, abruptly increasing the afterglow luminosity, which explains the sharp initial rise of the LHAASO light curve. Non-thermal emission by the pairs before their annihilation could have also contributed to the emission seen by *Fermi*/LAT at the same time. The observed properties of the line can be matched in our scenario provided that the circumstellar medium around the progenitor had a very high density, corresponding to a mass loss rate of about $10^{-3} - 10^{-1} M_\odot \text{ yr}^{-1}$ during the last few years before

the explosion, similar to what is inferred from studies of Type IIn supernovae. This provides a clue to the nature of the progenitor, the consequences of which are yet to be fully explored.

The mechanism described in this work might produce observable emission lines in other GRBs whose progenitor is surrounded by a dense circumstellar medium, if the jet emission features a long quiescence and provided that the GRB emission after the quiescence is very hard. These requirements can guide the search for similar emission lines in other sources.

Acknowledgements. O.S.S. thanks Sergio Campana for helpful discussions. This work has been funded by the European Union-Next Generation EU, PRIN 2022 RFF M4C21.1 (202298J7KT - PEACE). O.S.S. acknowledges funding from INAF through grant 1.05.23.04.04. G.G. acknowledges funding from INAF through grant 1.05.23.06.04.

References

- Axelsson, M., Ajello, M., Arimoto, M., et al. 2025, *ApJS*, 277, 24
- Band, D., Matteson, J., Ford, L., et al. 1993, *ApJ*, 413, 281
- Beloborodov, A. M. 2002, *ApJ*, 565, 808
- Blanchard, P. K., Villar, V. A., Chornock, R., et al. 2024, *Nature Astronomy*, 8, 774
- Blandford, R. D. & McKee, C. F. 1976, *Physics of Fluids*, 19, 1130
- Burns, E., Lesage, S., Goldstein, A., et al. 2024, arXiv e-prints, arXiv:2410.00286
- Chevalier, R. A. 2012, *ApJ*, 752, L2
- Chevalier, R. A. & Li, Z.-Y. 2000, *ApJ*, 536, 195
- Chugai, N. N., Blinnikov, S. I., Cumming, R. J., et al. 2004, *MNRAS*, 352, 1213
- Foreman-Mackey, D., Hogg, D. W., Lang, D., & Goodman, J. 2013, *PASP*, 125, 306
- Frederiks, D., Svinkin, D., Lysenko, A. L., et al. 2023, *ApJ*, 949, L7
- Fulton, M. D., Smartt, S. J., Rhodes, L., et al. 2023, *ApJ*, 946, L22
- Galama, T. J., Vreeswijk, P. M., van Paradijs, J., et al. 1998, *Nature*, 395, 670
- Gao, D.-Y. & Zou, Y.-C. 2023, *ApJ*, 956, L38
- Ghisellini, G. 2013, *Radiative Processes in High Energy Astrophysics* (Springer, Cham Heidelberg New York Dordrecht London)
- Gould, R. J. & Schréder, G. P. 1967, *Physical Review*, 155, 1404
- Jauch, J. M. & Rohrlich, F. 1976, *The theory of photons and electrons. The relativistic quantum field theory of charged particles with spin one-half* (Springer-Verlag, Berlin Heidelberg New York)
- Kiewe, M., Gal-Yam, A., Arcavi, I., et al. 2012, *ApJ*, 744, 10
- Kong, D.-F., Wang, X.-G., Zheng, W., et al. 2024, *ApJ*, 971, 56
- Kumar, P. & Panaiteescu, A. 2000, *ApJ*, 541, L51
- Kumar, P. & Zhang, B. 2015, *Phys. Rep.*, 561, 1
- Lesage, S., Veres, P., Briggs, M. S., et al. 2023, *ApJ*, 952, L42
- Levan, A. J., Lamb, G. P., Schneider, B., et al. 2023, *ApJ*, 946, L28
- LHAASO Collaboration, Cao, Z., Aharonian, F., et al. 2023, *Science*, 380, 1390
- Liu, J., Mao, J., Xiong, S.-L., & Zhang, Y.-Q. 2025, *ApJ*, 991, 204
- Madau, P. & Thompson, C. 2000, *ApJ*, 534, 239
- Malesani, D. B., Levan, A. J., Izzo, L., et al. 2025, *A&A*, 701, A134
- Panaiteescu, A. & Kumar, P. 2000, *ApJ*, 543, 66
- Pe'er, A. & Zhang, B. 2024, *ApJ*, 973, L51
- Planck Collaboration, Aghanim, N., Akrami, Y., et al. 2020, *A&A*, 641, A6
- Ravasio, M. E., Salafia, O. S., Oganesyan, G., et al. 2024, *Science*, 385, 452
- Salafia, O. S., Ghisellini, G., Pescalli, A., Ghirlanda, G., & Nappo, F. 2015, *MNRAS*, 450, 3549
- Sari, R. & Piran, T. 1995, *ApJ*, 455, L143
- Schlegel, E. M. 1990, *MNRAS*, 244, 269
- Sironi, L., Spitkovsky, A., & Arons, J. 2013, *ApJ*, 771, 54
- Srinivasaragavan, G. P., O'Connor, B., Cenko, S. B., et al. 2023, *ApJ*, 949, L39
- Svensson, R. 1987, *MNRAS*, 227, 403
- Thompson, C. & Madau, P. 2000, *ApJ*, 538, 105
- Thorne, K. S. & Zytkow, A. N. 1977, *ApJ*, 212, 832
- Vergani, S. D., Salvaterra, R., Japelj, J., et al. 2015, *A&A*, 581, A102
- Zhang, Y.-Q., Xiong, S.-L., Mao, J.-R., et al. 2024a, *Science China Physics, Mechanics, and Astronomy*, 67, 289511
- Zhang, Z., Lin, H., Li, Z., et al. 2024b, *ApJ*, 973, L17

Appendix A: Derivation of the high latitude emission effect

Let us assume the source to be a spherically symmetric, geometrically thin shell of comoving thickness $\Delta r'$ expanding with a bulk Lorentz factor Γ , and let us call $I(\theta)$ the bolometric intensity (surface brightness) at latitude θ (angle between the normal to the source surface and the axis parallel to the line of sight). Assuming for simplicity the source to be optically thin (the result does not change in the optically thick case), we can relate the intensity to the comoving bolometric emissivity j' by $I(\theta) = \mathcal{D}^4(\theta)j'\Delta r'$ (e.g. Ghisellini 2013), where

$$\mathcal{D}(\theta) = \frac{1}{\Gamma(1 - \beta \cos \theta)} \quad (\text{A.1})$$

is the Doppler factor, and $\beta = \sqrt{1 - \Gamma^{-2}}$. The total fluence (i.e. time-integrated flux) received by an observer at a luminosity distance d_L , neglecting cosmological redshift terms, is

$$\mathcal{F} = \frac{r^2}{d_L^2} \iint \Delta t_{\text{obs}}(\theta) I(\theta) \sin \theta d\theta d\phi, \quad (\text{A.2})$$

where $\Delta t_{\text{obs}}(\theta) = (1 - \beta \cos \theta)\Delta t_{\text{em}} = \Delta t_{\text{em}}/\Gamma\mathcal{D}(\theta)$ is the observed emission duration at latitude θ , and we assumed that r does not change appreciably during the emission (because $\Delta t_{\text{em}} \ll r/c$). We thus have

$$E_{\text{iso}} = 4\pi d_L^2 \mathcal{F} = \iint \frac{\mathcal{D}^3(\theta)}{\Gamma} 4\pi r^2 \Delta r' j' \Delta t_{\text{em}} \sin \theta d\theta d\phi. \quad (\text{A.3})$$

Since $4\pi r^2 \Delta r' = V'$ is the total source volume in the comoving frame, we have $V' j' \Delta t_{\text{em}} = L' \Delta t_{\text{em}}/4\pi = L \Delta t_{\text{em}}/4\pi = E/4\pi$, where L is the source luminosity, E is the total emitted energy, and we exploited the relativistic invariance of the emitted³ luminosity $L' = L$. Defining $dE/d\Omega = E/4\pi$ as the energy emitted per unit solid angle by the source, we finally have

$$E_{\text{iso}} = \iint \frac{\mathcal{D}^3(\theta)}{\Gamma} \frac{dE}{d\Omega} \sin \theta d\theta d\phi, \quad (\text{A.4})$$

which corresponds to the result already derived in Salafia et al. (2015). The differential isotropic equivalent energy contributed by each ‘ring’ of solid angle $d\Omega(\theta) = 2\pi \sin \theta d\theta$ is therefore

$$\frac{\partial E_{\text{iso}}}{\partial \Omega}(\theta) = \frac{\mathcal{D}^3(\theta)}{\Gamma} \frac{dE}{d\Omega}. \quad (\text{A.5})$$

When the HLE effect dominates the observed time evolution of the emission, a single such ring contributes to the observed emission at each time. The arrival time of photons from the latitude θ of the ring is

$$t_{\text{obs}}(\theta) - t_0 = \frac{r}{c}(1 - \cos \theta), \quad (\text{A.6})$$

where t_0 is the arrival time of the first photon. This can be solved for $\cos \theta$ and substituted into the Doppler factor definition, leading to

$$\mathcal{D}(t_{\text{obs}}) = \frac{\Gamma r}{\Gamma^2 c (t_{\text{obs}} - t_0 + r/(1 + \beta)\Gamma^2 c)} \equiv \frac{(1 + \beta)\Gamma}{1 + (t_{\text{obs}} - t_0)/t_{\text{ang}}}, \quad (\text{A.7})$$

where we have defined the ‘angular time scale’ $t_{\text{ang}} = r/(1 + \beta)\Gamma^2 c$. This establishes a one-to-one correspondence between each ring and its associated Doppler factor: the observed time evolution also corresponds to a monotonic decrease in Doppler boosting.

Differentiating Eq. A.6 with respect to $d\Omega = -2\pi d \cos \theta$, we also obtain

$$\frac{\partial t_{\text{obs}}}{\partial \Omega} = \frac{r}{2\pi c}, \quad (\text{A.8})$$

which encodes the fact that photons emitted over a differential range of latitudes $(\cos \theta, \cos \theta - \sin \theta d\theta)$ reach the observer over a range of times $(t_{\text{obs}}(\theta), t_{\text{obs}}(\theta) + r \sin \theta d\theta/c)$. This leads to

$$L_{\text{iso}}(t_{\text{obs}}) = \frac{\partial \Omega}{\partial t_{\text{obs}}} \frac{\partial E_{\text{iso}}}{\partial \Omega} = \frac{2\pi c}{r} \cdot \frac{E}{4\pi} \cdot \frac{(1 + \beta)^3 \Gamma^3}{\Gamma [1 + (t_{\text{obs}} - t_0)/t_{\text{ang}}]^3}. \quad (\text{A.9})$$

Using $\beta \approx 1$ and rearranging terms, we get to the final expression for the HLE luminosity evolution, namely

$$L_{\text{iso}}(t_{\text{obs}}) \sim \frac{2E/t_{\text{ang}}}{[1 + (t_{\text{obs}} - t_0)/t_{\text{ang}}]^3}, \quad (\text{A.10})$$

³ The *observed* isotropic-equivalent luminosity, on the other hand, is not an invariant.

which holds until $t_{\text{obs}} - t_0 = 2r/c$ (see Eq. A.6), after which the luminosity goes to zero. This shows that the HLE effect wipes out the information on the intrinsic luminosity of the emission process (and clearly also any evolution on time scales shorter than the angular time scale), producing a nearly constant luminosity over a time t_{ang} followed by a rapid decay $L_{\text{iso}} \propto (t_{\text{obs}} - t_0)^{-3}$. The initial luminosity is twice the total emitted energy divided by the angular time scale. The above derivation demonstrates that the results presented by Pe'er & Zhang (2024), which are based on the assumption that the observed luminosity and the comoving one are related by $L_{\text{iso}} = \mathcal{D}^2 L'$, may need to be revised.

The Doppler factor evolution, Eq. A.7, also sets the spectral evolution, since any frequency evolves as

$$h\nu_{\text{obs}} = \mathcal{D}(t_{\text{obs}})h\nu' = \frac{h\nu_{\text{obs},0}}{1 + (t_{\text{obs}} - t_0)/t_{\text{ang}}}, \quad (\text{A.11})$$

where ν' is the comoving frequency and $\nu_{\text{obs},0} = (1 + \beta)\Gamma\nu'$. If $F_\nu(\nu_{\text{obs}}, t_0)$ is the spectrum at time t_0 , then at a later time

$$F_\nu(\nu_{\text{obs}}, t_{\text{obs}}) = \frac{F_\nu\left(\left(1 + (t_{\text{obs}} - t_0)/t_{\text{ang}}\right)\nu_{\text{obs}}, t_0\right)}{\left[1 + (t_{\text{obs}} - t_0)/t_{\text{ang}}\right]^2}, \quad (\text{A.12})$$

where the term at the denominator follows from the requirement that $\nu_{\text{obs}}F_\nu \propto L_{\text{iso}}$, where the isotropic-equivalent luminosity evolves as predicted by Eq. 1. Assuming a power law spectrum, $F_\nu(\nu_{\text{obs}}, t_0) \propto \nu_{\text{obs}}^{-\beta}$, and focussing on $t_{\text{obs}} \gg t_{\text{ang}}$, we recover the original result of Kumar & Panaiteescu (2000), namely

$$F_\nu(\nu_{\text{obs}}, t_{\text{obs}}) \propto \nu_{\text{obs}}^{-\beta} t_{\text{obs}}^{-(2+\beta)}. \quad (\text{A.13})$$

Appendix B: HLE model fitting

In this appendix we describe the technical details of our procedure for fitting the HLE model to the line properties inferred from the observations. In order to account for the inherent degeneracies in the model, we re-parametrised it by defining the parameter vector $\mathbf{x} = (x_0, x_1, x_2, x_3)$, with

$$\begin{aligned} x_0 &= r, \\ x_1 &= \Gamma/r, \\ x_2 &= N_\pm/r, \\ x_3 &= t_0\Gamma^2/r \propto t_0/t_{\text{ang}}. \end{aligned} \quad (\text{B.1})$$

Each line luminosity and central photon energy error bar from the literature has been inferred using data from a relatively long time bin $[t_a, t_b]$. In order to compare the model with these properties, we defined the model mean luminosity as

$$\langle L_{\text{line}} \rangle_{[t_a, t_b]}(\mathbf{x}) = \frac{\int_{t_a}^{t_b} L_{\text{line}}(t_{\text{obs}}, \mathbf{x}) dt_{\text{obs}}}{t_b - t_a}, \quad (\text{B.2})$$

and the model mean line photon energy as

$$\langle h\nu_{\text{line}} \rangle_{[t_a, t_b]}(\mathbf{x}) = \frac{\int_{t_a}^{t_b} L_{\text{line}}(t_{\text{obs}}, \mathbf{x}) h\nu_{\text{line}}(t_{\text{obs}}, \mathbf{x}) dt_{\text{obs}}}{\int_{t_a}^{t_b} L_{\text{line}}(t_{\text{obs}}, \mathbf{x}) dt_{\text{obs}}}. \quad (\text{B.3})$$

Let the i -th error bar be characterised by an inferred line luminosity $L_{i-\delta L_{i,\text{low}}}^{+\delta L_{i,\text{high}}}$ and central photon energy $h\nu_{i-\delta h\nu_{i,\text{low}}}^{+\delta h\nu_{i,\text{high}}}$, where the sub- and super-scripts indicate one-sigma errors. We defined the additive contribution of this error bar to the log-likelihood as

$$\ln \mathcal{L}_i(\mathbf{x}) = -\frac{1}{2} \left\{ \left[\frac{\langle L_{\text{line}} \rangle_{[t_a, t_b]}(\mathbf{x}) - L_i}{\delta L_i(\mathbf{x})} \right]^2 + \left[\frac{\langle h\nu_{\text{line}} \rangle_{[t_a, t_b]}(\mathbf{x}) - h\nu_i}{\delta h\nu_i(\mathbf{x})} \right]^2 \right\}, \quad (\text{B.4})$$

where

$$\delta L_i(\mathbf{x}) = \begin{cases} \delta L_{i,\text{high}} & \text{if } \langle L_{\text{line}} \rangle_{[t_a, t_b]}(\mathbf{x}) \geq L_i \\ \delta L_{i,\text{low}} & \text{otherwise} \end{cases}, \quad (\text{B.5})$$

and similarly

$$\delta h\nu_i(\mathbf{x}) = \begin{cases} \delta h\nu_{i,\text{high}} & \text{if } \langle h\nu_{\text{line}} \rangle_{[t_a, t_b]}(\mathbf{x}) \geq h\nu_i \\ \delta h\nu_{i,\text{low}} & \text{otherwise} \end{cases}. \quad (\text{B.6})$$

For luminosity upper limits, we simply set L_i equal to the 2-sigma upper limit value, $\delta L_{i,\text{high}} = 0$ and $\delta L_{i,\text{low}} = \infty$. We assumed log-uniform priors on all parameters, that is, $\pi(\mathbf{x}) = \prod_{i=0}^3 x_i^{-1}$. Therefore, our posterior probability density took the form

$$p(\mathbf{x} | \mathbf{d}) \propto \prod_{i=0}^3 x_i^{-1} \exp \left[\sum_{j=1}^N \ln \mathcal{L}_j(\mathbf{x}) \right], \quad (\text{B.7})$$

where N is the number of considered error bars. We sampled this posterior probability density using the emcee python package (Foreman-Mackey et al. 2013), then we reconstructed the posterior probability densities of the original parameters $\mathbf{x}' = (r, \Gamma, N_\pm, t_0)$ by transforming each sample \mathbf{x}_i to the original base, $\mathbf{x}'_i = T^{-1}(\mathbf{x}_i)$, where T^{-1} is the solution to the system of equations B.1.

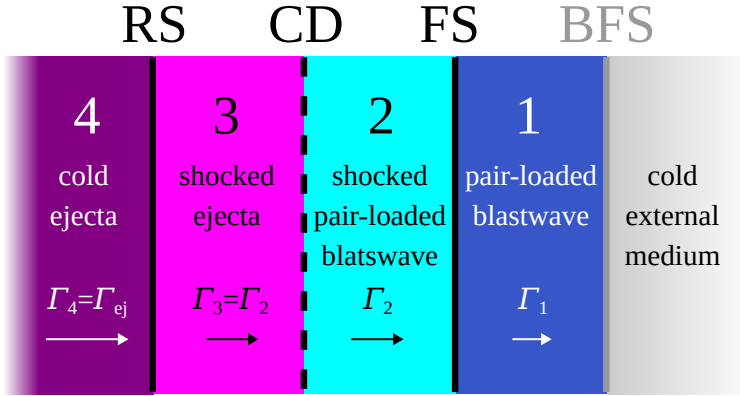


Fig. C.1. Configuration of the system after the main event ejecta collide with the pair-loaded blastwave, before the forward shock (FS) that arises from the collision crosses the pair-loaded blastwave, catching up with the pre-existing blastwave forward shock (BFS). The reverse shock (RS) separates the cold main event ejecta from the shocked part. A contact discontinuity (CD) separates the ejecta from the the pair-loaded blastwave material.

Appendix C: Hydrodynamical acceleration after ejecta collision

When the ejecta reach the pair-loaded blastwave, unless the latter has been radiatively accelerated to a bulk Lorentz factor $\Gamma_1 \gtrsim \Gamma_{\text{ej}}$, a violent collision takes place, with the formation of a forward and a reverse shock (RS). The forward shock (FS) first crosses the pair-loaded blastwave, then propagates into the external medium. In the first of these two phases, sketched in Fig. C.1, four regions are relevant to the dynamics: (1) the pair-loaded blastwave, (2) the shocked, pair-loaded blastwave, (3) the shocked ejecta and (4) the un-perturbed ejecta. Regions 1 and 2 are separated by the FS; regions 3 and 4 are separated by the RS; a contact discontinuity (CD) separates regions 2 and 3. Regions 2 and 3 move at the same speed, hence the pressure must balance on the two sides of the contact discontinuity. This can be used (e.g. Sari & Piran 1995) to derive the bulk Lorentz factor of regions 2-3, as follows. Let us define the ratio ℓ of the gamma-ray luminosity L to the kinetic luminosity L_{ej} of the main event ejecta (after the gamma-rays are released), so that $L = \ell L_{\text{ej}}$. This implies a main event gamma-ray efficiency of $\eta_\gamma = L/(L + L_{\text{ej}}) = \ell/(1 + \ell)$. The comoving rest-mass density in region 4 is then $\rho'_4 \sim L_{\text{ej}}/4\pi r_0^2 \Gamma_{\text{ej}}^2 c^3 = L/4\pi r_0^2 \Gamma_{\text{ej}}^2 c^3 \ell$. Calling Γ_2 the bulk Lorentz factor of regions 2-3, and assuming $\Gamma_2 \ll \Gamma_{\text{ej}}$, the relative Lorentz factor between regions 3 and 4 is $\Gamma_{34} \sim \Gamma_{\text{ej}}/2\Gamma_2$. The relativistic Rankine-Hugoniot shock jump conditions (BM76) then set the pressure in region 3, $p_3 \sim 4\Gamma_{34}^2 \rho'_4 c^2/3$. Similarly, the pressure in region 2 is $p_2 \sim 4\Gamma_{12}^2 \rho'_1 c^2/3$: the relative Lorentz factor can be expressed as $\Gamma_{12} \sim \Gamma_2/2\zeta_{\text{racc}}\Gamma_0$, where we assumed that prior to the collision the pair loaded shell had a bulk Lorentz factor $\Gamma_1 = \zeta_{\text{racc}}\Gamma_0$. Before being irradiated, the blastwave had a number density (just behind the shock) $n'_{1,0} \sim 4\Gamma_0 n_{\text{ext}}(r_0)$. After the radiative acceleration, this density becomes $n'_1 \sim 4\zeta_{\text{racc}}\Gamma_0 n_{\text{ext}}(r_0)$ (Madau & Thompson 2000; Beloborodov 2002, see also Appendix D.2). Assuming the shell rest mass to be pair-dominated ($Z_\pm \gtrsim m_p/2m_e$), the density is then $\rho'_1 \sim Z_\pm n'_1 m_e$. Requiring $p_2 = p_3$, we obtain the Lorentz factor of the shocked pair-loaded shell

$$\Gamma_2 \sim \left[\frac{L \zeta_{\text{racc}} \Gamma_0}{16\pi r_0^2 c \ell Z_\pm n_{\text{ext}}(r_0) m_e c^2} \right]^{1/4}. \quad (\text{C.1})$$

Imposing $Z_\pm = Z_{\pm, \text{HLE}}$ and substituting r_0 and Γ_0 with the expressions in Eqs. 12 and 14, we obtain

$$\Gamma_2 \approx \left(\frac{(1+z)h\nu_{\text{line}}}{14.5 \text{ MeV}} \right)^{3/4} L_{\text{line},50}^{-1/4} \zeta_{\text{racc}}^{1/4} L_{52.6}^{1/4} \ell_{-1}^{-1/4} \times \begin{cases} 190 Y_e^{1/4} E_{\text{pre},52}^{1/32} n_{\text{ext},2}^{-1/32} \Delta t_{\text{pre},2.2}^{-3/32} & k = 0; \\ 155 Y_e^{1/4} E_{\text{pre},52}^{1/16} A_{\star,0}^{-1/16} \Delta t_{\text{pre},2.2}^{-1/16} & k = 2. \end{cases} \quad (\text{C.2})$$

If the pair mass-annihilation happens in this phase, then we have also the requirement $\Gamma_2 = \Gamma_{\text{HLE}}$ (Eq. 6). In this case, we obtain a constraint on ℓ , namely

$$\ell \approx \left(\frac{(1+z)}{1.15} \right)^3 \left(\frac{h\nu_{\text{line}}}{12.6 \text{ MeV}} \right)^7 \left(\frac{t_{\text{line}} - t_0}{60 \text{ s}} \right)^4 L_{\text{line},50}^{-1} L_{52.6} \times \begin{cases} 3.1 \times 10^{-4} \zeta_{\text{racc}} Y_e E_{\text{pre},52}^{-7/8} n_{\text{ext},2}^{7/8} \Delta t_{\text{pre},2.2}^{-11/8} & k = 0; \\ 0.01 \zeta_{\text{racc}} Y_e E_{\text{pre},52}^{-7/4} A_{\star,0}^{7/4} \Delta t_{\text{pre},2.2}^{-9/4} & k = 2. \end{cases} \quad (\text{C.3})$$

When $\ell \ll 1$, the above constraint is equivalent to that on the prompt emission efficiency of the main event, η_γ . Large values $\ell > 1$ imply large prompt emission efficiencies $\eta_\gamma > 0.5$.

These calculations show that, in principle, the mass-annihilation of the pairs (that is, the pair bubble bursting) could happen after the collision between the main event ejecta and the pair-enriched blastwave. If this is the case, the kinetic energy of the main event ejecta must satisfy a constraint in order to accelerate the pair bubble to the Lorentz factor required by HLE.

A relevant question is whether the pairs would annihilate entirely during this phase, or else their annihilation time is longer than the time scale for the shock to cross the pair-loaded shell. A simple calculation shows that the shock crossing time, as measured in the lab frame, is on the order of r_0/c . Therefore, the requirement imposed by HLE on the annihilation time scale (that needs be shorter than r_0/c) automatically implies that the pairs must annihilate during this phase.

Appendix D: Detailed modelling of the interaction between incident gamma-ray photons and the blastwave

In this appendix we derive our pair enrichment and radiative acceleration model. The results are very similar to Be02, with some subtle difference, as discussed below.

Appendix D.1: Pair enrichment rate

Let us consider a homogeneous shell of radius r expanding at a speed β (in units of the speed of light c , hence with an associated bulk Lorentz factor Γ), containing number densities n_e and n_{\pm} of cold electrons and pairs, respectively, that is illuminated by a central source of gamma-rays with a flux $F_{\varepsilon} = L_e/4\pi r^2$ (here $\varepsilon = h\nu/m_e c^2$ is an incident photon energy in units of the electron rest mass energy, and L_e is the specific luminosity of the central source). The specific number density of incident photons is $dn_{\gamma}/d\varepsilon = L_e/4\pi r^2 \varepsilon m_e c^3 = F_{\varepsilon}/\varepsilon m_e c^3$.

Leptons can Compton-scatter these incident photons. In the lepton rest frame, the differential scattering cross section for incident photons of energy $\varepsilon' = \varepsilon/(1+\beta)\Gamma$ scattered to an angle whose cosine is $\mu' = (\mu-\beta)/(1-\beta\mu)$ is the Klein-Nishina cross section (Jauch & Rohrlich 1976),

$$\frac{d\sigma_{\text{KN}}}{d\Omega'} = \frac{3\sigma_T}{16\pi} \cdot \frac{\varepsilon'(1-\mu') + \mu'^2 + [1 + \varepsilon'(1-\mu')]}{[1 + \varepsilon'(1-\mu')]^2}. \quad (\text{D.1})$$

Since the total cross section is a relativistic invariant, the lab-frame differential cross section is obtained by transforming only the solid angle, so that

$$\frac{d\sigma_{\text{KN}}}{d\Omega}(\varepsilon, \mu) = \mathcal{D}^2(\mu) \frac{d\sigma_{\text{KN}}}{d\Omega'}(\varepsilon', \mu'). \quad (\text{D.2})$$

The differential scattering rate density for a single lepton is therefore

$$\frac{d^3N_{\text{sc}}}{dt d\varepsilon d\Omega}(\varepsilon, \mu) = \frac{d\sigma_{\text{KN}}}{d\Omega}(\varepsilon, \mu)(1-\beta)c \frac{dn_{\gamma}}{d\varepsilon}(\varepsilon), \quad (\text{D.3})$$

where the $1-\beta$ term accounts for the relative velocity between the lepton and the incident photons. In the pre-scattering rest frame of the lepton, the photon energy after scattering, from conservation of momentum and energy, is

$$\varepsilon'_{\text{sc}} = \frac{\varepsilon'}{1 + (1-\mu')\varepsilon'}. \quad (\text{D.4})$$

In the lab-frame, this becomes

$$\varepsilon_{\text{sc}} = \frac{(1-\beta)\varepsilon}{1 - \beta\mu + (1-\mu)\varepsilon/\Gamma}. \quad (\text{D.5})$$

The differential scattering rate density in terms of the scattered photon energy is then

$$\frac{d^3N_{\text{sc}}}{dt d\varepsilon_{\text{sc}} d\Omega}(\varepsilon_{\text{sc}}, \mu) = \frac{\partial\varepsilon}{\partial\varepsilon_{\text{sc}}} \cdot \frac{d\sigma_{\text{KN}}}{d\Omega}(\varepsilon, \mu)(1-\beta)c \frac{dn_{\gamma}}{d\varepsilon}(\varepsilon) = \frac{\partial\varepsilon}{\partial\varepsilon_{\text{sc}}} \cdot \mathcal{D}^2(\mu) \frac{d\sigma_{\text{KN}}}{d\Omega'} \left(\frac{\varepsilon}{(1+\beta)\Gamma}, \frac{\mu-\beta}{1-\beta\mu} \right) (1-\beta) \frac{F_{\varepsilon}(\varepsilon)}{\varepsilon m_e c^2}. \quad (\text{D.6})$$

Let us now focus on photons scattered within a time $(t_{\text{sc}}, t_{\text{sc}} + dt_{\text{sc}})$ to energies within $(\varepsilon_{\text{sc}}, \varepsilon_{\text{sc}} + d\varepsilon_{\text{sc}})$ and angles within $(\mu, \mu + d\mu)$, and evaluate their number density at a time t . Their initial density is proportional to that of the scattering centers, but reduced by a $(1-\beta)$ factor because the latter move during the time interval dt_{sc} , so that

$$\frac{d^3n_{\text{sc}}}{d\varepsilon_{\text{sc}} d\Omega dt_{\text{sc}}}(t = t_{\text{sc}}, t_{\text{sc}}, \varepsilon_{\text{sc}}, \mu) d\varepsilon_{\text{sc}} d\Omega dt_{\text{sc}} \sim (1-\beta) [n_e(t_{\text{sc}}) + 2n_{\pm}(t_{\text{sc}})] \frac{d^3N_{\text{sc}}}{dt d\varepsilon_{\text{sc}} d\Omega}(\varepsilon_{\text{sc}}, \mu, t_{\text{sc}}) d\varepsilon_{\text{sc}} d\Omega dt_{\text{sc}}. \quad (\text{D.7})$$

At a later time t , the photons will have travelled to $r(t) = r + \mu c(t - t_{\text{sc}})$, but since the process of interest happens over a time $t - t_{\text{sc}} \ll r/c$ (which is also a condition for our planar treatment to remain strictly valid), this dilution can be ignored. Still, an additional process modifies the photon number density with time: during their flight, some of the scattered photons interact with incident photons and annihilate to produce electron positron pairs. Let us indicate with $\lambda_{\gamma\gamma}(\varepsilon_{\text{sc}}, \mu)$ the mean free path of a scattered photon before undergoing such an annihilation. The average pair production time for each of these photons is $\lambda_{\gamma\gamma}/c$, and at time t the number of photons that survived such annihilations is lower by a factor $\exp(-c(t - t_{\text{sc}})/\lambda_{\gamma\gamma})$ with respect to the initial scattered photons. Hence the differential pair production rate density by the annihilation of these photons at time t is

$$\frac{d^3\dot{n}_{\pm, \gamma\gamma}}{d\varepsilon_{\text{sc}} d\Omega dt_{\text{sc}}}(t, \varepsilon_{\text{sc}}, \mu) \sim \frac{d^3n_{\text{sc}}}{d\varepsilon_{\text{sc}} d\Omega dt_{\text{sc}}}(t, t_{\text{sc}}, \varepsilon_{\text{sc}}, \mu) \frac{c}{\lambda_{\gamma\gamma}(\varepsilon, \mu)} = (1-\beta) [n_e(t_{\text{sc}}) + 2n_{\pm}(t_{\text{sc}})] \frac{d^3N_{\text{sc}}}{dt d\varepsilon_{\text{sc}} d\Omega}(\varepsilon_{\text{sc}}, \mu, t_{\text{sc}}) e^{-\frac{c(t-t_{\text{sc}})}{\lambda_{\gamma\gamma}(\varepsilon_{\text{sc}}, \mu)}} \frac{c}{\lambda_{\gamma\gamma}(\varepsilon_{\text{sc}}, \mu)}. \quad (\text{D.8})$$

Setting $n^* = (n_e + 2n_{\pm})(1-\beta)$ and $dw_{\text{sc}} = (1-\beta)c dt_{\text{sc}} = d(ct_{\text{sc}} - r)$ and integrating over all scattering times $0 < t_{\text{sc}} < t$ (so that $t = 0$ is the time when the shell starts being illuminated), scattering angles and photon energies, after changing one integration variable from ε_{sc} to ε , we obtain the total pair production rate density at time t ,

$$\dot{n}_{\pm, \gamma\gamma}(t) = 2\pi \int_0^{w(t)} dw_{\text{sc}} \int_{-1}^1 d\mu \mathcal{D}^2(\mu, t_{\text{sc}}) \int_0^{\infty} d\varepsilon \frac{F_{\varepsilon}(\varepsilon)}{\varepsilon m_e c^2} n^*(w_{\text{sc}}) \frac{d\sigma_{\text{KN}}}{d\Omega'} \left(\frac{\varepsilon}{(1+\beta)\Gamma}, \frac{\mu-\beta}{1-\beta\mu} \right) \frac{e^{-\frac{w-w_{\text{sc}}}{\lambda_{\gamma\gamma}(\varepsilon_{\text{sc}}, \mu)}}}{\lambda_{\gamma\gamma}(\varepsilon_{\text{sc}}, \mu)}. \quad (\text{D.9})$$

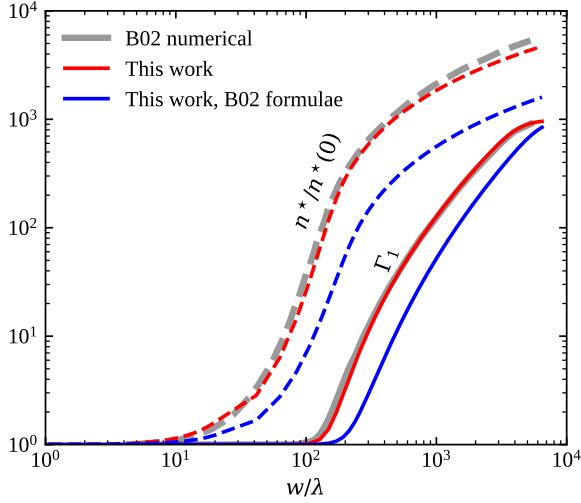


Fig. D.1. Comparison between our numerical results and those of Be02 for a cold and unperturbed shell at a radius $r = 10^{14}$ cm illuminated by a central source with $L = 10^{51}$ erg/s with a broken power law spectrum peaking at $\varepsilon_p = 1$ and with slopes $\alpha_1 = 1$ and $\alpha_2 = 2.5$. Dashed lines show the lepton density evolution ($n^*/n^*(0)$), while solid lines show the bulk Lorentz factor Γ_1 of the illuminated region, as a function of w/λ , where $\lambda = 4\pi r^2 m_e c^3 / \sigma_T L$ is the electron mean free path for Thomson scattering. Numerical results from Be02 (taken from their figure 1) are shown in grey. Results from our model (neglecting pair annihilation) are shown in red. Results obtained using the formulae as written in Be02 are shown in blue.

The $\lambda_{\gamma\gamma}$ mean free path is given by (Gould & Schréder 1967)

$$\lambda_{\gamma\gamma}^{-1}(\varepsilon_{\text{sc}}, \mu) = \int_{\varepsilon_{\text{th}}}^{+\infty} (1 - \mu) \sigma_{\gamma\gamma}(\varepsilon_{\text{sc}}, \varepsilon, \mu) \frac{dn_\gamma}{d\varepsilon} d\varepsilon, \quad (\text{D.10})$$

where ε represents again the energy of an incident photon, $\varepsilon_{\text{th}} = 2/(1 - \mu)\varepsilon_{\text{sc}}$ is the threshold for $\gamma - \gamma$ absorption, and

$$\sigma_{\gamma\gamma}(\varepsilon, \varepsilon_{\text{sc}}, \mu) = \frac{3\sigma_T}{8x^2} \left[(2 + 2x^{-2} - x^{-4}) \ln(x + \sqrt{x^2 - 1}) - (1 + x^{-2}) \sqrt{1 - x^{-2}} \right] \quad (\text{D.11})$$

is the Breit-Wheeler cross section (Jauch & Rohrlich 1976), with $x = \sqrt{\varepsilon\varepsilon_{\text{sc}}(1 - \mu)/2}$.

We note that our Eq. D.9 differs from equation 8 of Be02 because of an additional $\partial\varepsilon_{\text{sc}}/\partial\varepsilon$ factor (similarly for Eq. D.14). Also, our Eq. D.10 contains a $(1 - \mu)$ factor that is not present in equation A7 of Be02 (but it is present in Gould & Schréder 1967). Still, our numerical results reproduce very well those of Be02 (see the comparison between grey and red lines Fig. D.1), which suggests that these differences are only due to misprints in that work. This is further supported by the fact that, when using the forms of the equations as given in Be02, we cannot reproduce their results (blue lines in Fig. D.1).

Appendix D.2: Pair density evolution and radiative acceleration

The auxiliary variable $w = ct - r$ represents the radial distance at time t between the outer edge of the gamma-ray front and the region of interest (Be02). We note that $w(t) = cE_{\gamma\text{f}}(t)/L$, hence wL/c also represents the amount of radiative energy that crossed the region of interest at time t . In the lab-frame, the number density $n = n_e + 2n_{\pm}$ evolves with the w variable according to the continuity equation (Be02)

$$c \frac{\partial}{\partial w} [n(1 - \beta)] = 2(\dot{n}_{\pm, \gamma\gamma} - \dot{n}_{\pm, \text{ann}}), \quad (\text{D.12})$$

where $\dot{n}_{\pm, \text{ann}} = 3\sigma_T c n_{\pm}^2 / 8\Gamma^2$ is the pair annihilation rate. Differently from Be02, we keep this term as it is not negligible in our context. Because the source term only affects the pair density, the above equation implies that the density of original electrons satisfies $n_e^*(w) = n_e(w)(1 - \beta(w)) = n_e(0)(1 - \beta(0))$ and is therefore a conserved quantity (Madau & Thompson 2000). In order to describe the radiative acceleration, we exploit the momentum conservation equation (Be02)

$$c^2 \frac{\partial}{\partial w} [\beta \Gamma \rho(1 - \beta)] = \dot{P}_{\pm} + \dot{P}_{\text{sc}} + \dot{P}_{\text{ann}}, \quad (\text{D.13})$$

where $\rho = Y_e^{-1} m_p n_e + m_e n$ is the rest-mass density (Y_e^{-1} being the average number of nucleons per electron in the medium), \dot{P}_{\pm} is the momentum deposition rate per unit volume due to pair creation, \dot{P}_{sc} is that due to Compton scattering, and \dot{P}_{ann} is that due to the emission of pair annihilation photons. To compute the first, we assume that the entire momentum of each created pair is deposited into the fluid, due to the presence of a magnetic field in the plasma. The momentum of the pair is equal to that of the annihilating photons, which is $p_{\pm} \sim (\mu\varepsilon_{\text{sc}} + \chi\varepsilon_{\text{th}}(\varepsilon_{\text{sc}}, \mu))m_e c$, where the quantity $\chi \sim 1$ (which is the ratio of the average absorbed photon energy to the threshold energy) is given in appendix A3 of Be02. Therefore

$$\dot{P}_{\pm}(w) \sim 2\pi \int_{-1}^1 \int \frac{d^2 \dot{n}_{\pm, \gamma\gamma}}{d\varepsilon_{\text{sc}} d\Omega}(\varepsilon_{\text{sc}}, \mu, w) p_{\pm}(\varepsilon_{\text{sc}}, \mu) d\varepsilon_{\text{sc}} d\mu, \quad (\text{D.14})$$

where

$$\frac{d^2\dot{n}_{\pm,\gamma\gamma}}{d\varepsilon_{sc}d\Omega}(\varepsilon_{sc},\mu,w) = \int_0^w \frac{d^3\dot{n}_{\pm,\gamma\gamma}}{d\varepsilon_{sc}d\Omega dt_s}(\varepsilon_{sc},\mu,t_s(w_s),t(w)) \frac{dw_s}{c}. \quad (D.15)$$

For what concerns the momentum deposition rate due to scattering, we start by computing the difference between the momentum carried by an incident photon, $p_{in} = \varepsilon m_e c$, and the momentum carried by the photon after being scattered, $p_{out} = \mu \varepsilon_{sc} m_e c$. Each scattering hence deposits a momentum $\Delta p = p_{in} - p_{out}$. The volumetric momentum deposition rate due to scattering is obtained by integrating this deposited momentum over the volumetric density of scatterings, namely

$$\dot{P}_{sc}(w) = 2\pi \iint \Delta p(\varepsilon_{sc},\mu) \frac{d^3\dot{n}_{sc}}{d\varepsilon_{sc}d\Omega dt_{sc}}(w,w_{sc}=w,\varepsilon,\mu) d\varepsilon_{sc}d\mu = 2\pi \int_{-1}^1 d\mu \mathcal{D}^2 \int_0^\infty d\varepsilon \frac{F_\varepsilon(\varepsilon)}{\varepsilon m_e c^2} n^*(w) \frac{d\sigma_{KN}}{d\Omega'} \left(\frac{\varepsilon}{(1+\beta)\Gamma}, \frac{\mu-\beta}{1-\beta\mu} \right) \Delta p(\varepsilon,\mu). \quad (D.16)$$

The volumetric momentum loss rate due to the emission of pair annihilation photons, which we include for completeness, is computed as

$$\dot{P}_{ann} \sim -2\Gamma\beta m_e c \dot{n}_{\pm,ann}, \quad (D.17)$$

where the approximation adopted stems from the fact that pair annihilation photons are preferentially emitted at $\mu' \sim 0$ in the comoving frame (assuming isotropic pairs), hence $\mu \sim \beta$.

Equations D.12 and D.13 can be used to evolve the conservative variables n_\pm^* , n_e^* and $\varrho^* = \beta\Gamma\rho(1-\beta)$. In order to compute in practice the evolution, at each step it is also necessary to compute the primitive variables n and Γ . To that purpose, we use the relation (which follows from the definitions of ρ^* , n^*)

$$\beta(w)\Gamma(w) = \frac{\varrho^*(w)}{Y_e^{-1}m_p n_e^*(0) + m_e n_e^*(w)}, \quad (D.18)$$

from which the bulk Lorentz factor is computed as $\Gamma(w) = \sqrt{1 + (\beta(w)\Gamma(w))^2}$.

The initial condition of Eq. D.12 is (cfr. Section 4.1)

$$n^*(0) = n_e^*(0) = (4\Gamma_0 + 3)\Gamma_0 Y_e n_{ext}(r_0)(1 - \beta_0), \quad (D.19)$$

where $\beta_0 = \sqrt{1 - \Gamma_0^{-2}}$. For Eq. D.13, the initial condition is

$$\rho^*(0) = \beta_0 \Gamma_0 (Y_e^{-1}m_p + m_e) n_e^*(0). \quad (D.20)$$

We integrate the differential equations with Euler's method. After the solution is computed, we obtain the pair multiplicity as a function of the gamma-ray energy of the illumination phase,

$$Z_\pm(E_{\gamma f}) = \left. \frac{n^*(w)}{n^*(0)} \right|_{w=cE_{\gamma f}/L}, \quad (D.21)$$

and the corresponding bulk Lorentz factor

$$\Gamma_1(E_{\gamma f}) = \Gamma(w)|_{w=cE_{\gamma f}/L}. \quad (D.22)$$

The number of pairs that annihilated is obtained as follows. First, the pair annihilation rate is expressed as

$$\dot{N}_{\pm,ann} = V \dot{n}_{\pm,ann} = \frac{3\sigma_{TC}}{8\Gamma^2} \cdot n_\pm \cdot N_\pm = \frac{3\sigma_{TC}}{8\Gamma^2} \cdot \frac{n_\pm^*}{1-\beta} \cdot \frac{Z_\pm}{2} N_e = \frac{3\sigma_{TC} N_e}{32} (1+\beta) (n^* - n_e^*) Z_\pm. \quad (D.23)$$

The expression is then integrated over $dt = dw/(1-\beta)c$ to obtain

$$N_{\pm,ann}(E_{\gamma f}) = \frac{3\sigma_{TC} N_e}{32} \int_0^{cE_{\gamma f}/L} (1+\beta(w))^2 \Gamma^2(w) (n^*(w) - n_e^*) Z_\pm(w) dw. \quad (D.24)$$